sustainability

Article

Machine Learning Techniques in Predicting Bottom Hole Temperature and Remote Sensing for Assessment of Geothermal Potential in the Kingdom of Saudi Arabia

Faisal Alqahtani [1,2], Muhsan Ehsan [3,*], Murad Abdulfarraj [1,2], Essam Aboud [2,*], Zohaib Naseer [3], Nabil N. El-Masry [2] and Mohamed F. Abdelwahed [2]

[1] Faculty of Earth Sciences, King Abdulaziz University, Jeddah 21589, Saudi Arabia; falqahtani@kau.edu.sa (F.A.); mmrajab@kau.edu.sa (M.A.)
[2] Geohazards Research Center, King Abdulaziz University, Jeddah 21589, Saudi Arabia; nelmasryn@gmail.com (N.N.E.-M.); mfarouk40@yahoo.com (M.F.A.)
[3] Department of Earth and Environmental Sciences, Bahria School of Engineering and Applied Sciences, Bahria University, Islamabad 44000, Pakistan
* Correspondence: muhsanehsan98@hotmail.com (M.E.); eaboudishish@kau.edu.sa (E.A.)

Abstract: The global demand for energy is increasing rapidly due to population growth, urbanization, and industrialization, as well as to meet the desire for a higher standard of living. However, environmental concerns, such as air pollution from fossil fuels, are becoming limiting factors for energy sources. Therefore, the appropriate and sustainable solution is to transition towards renewable energy sources to meet global energy demands by using environmentally friendly sources, such as geothermal. The Harrat Rahat volcanic field, located in the western region of the Kingdom of Saudi Arabia (KSA), gets more attention due to its geothermal potential as a viable site for geothermal energy exploration due to its high enthalpy. The prime objective of this study is to present up-to-date and comprehensive information on the utilization of borehole temperature and remote sensing data to identify the most prospective zones with significant geothermal activity favorable for exploration and drilling. A brief description of the selected wells and the methodology used to determine the petrophysical parameters relevant to the geothermal potential assessment are presented. Special emphasis is given to gamma-ray ray and temperature logs for calculating heat production and the geothermal gradient. The effectiveness of various machine learning techniques are assessed throughout this study for predicting the temperature-at-depth to evaluate the suitability of employing machine learning models for temperature prediction, and it is found that XG Boost provided excellent results. It can be observed that some linear anomalies can be traced in the NW, trending on the west side of the Harrat volcanic field based on magnetic data interpretation. The land surface temperature in 2021 exhibited higher temperatures compared to 2000, suggesting potential volcanic activity in the subsurface. It is concluded that the integration of remote sensing data with subsurface data provides the most reliable results.

Keywords: renewable energy; geothermal resources; remote sensing; LST; magnetic data temperature; borehole temperature

check for updates

Citation: Alqahtani, F.; Ehsan, M.; Abdulfarraj, M.; Aboud, E.; Naseer, Z.; El-Masry, N.N.; Abdelwahed, M.F. Machine Learning Techniques in Predicting Bottom Hole Temperature and Remote Sensing for Assessment of Geothermal Potential in the Kingdom of Saudi Arabia. *Sustainability* **2023**, *15*, 12718. https://doi.org/10.3390/su151712718

Academic Editors: Wen Zhang, Chen Cao, Jie Dou and Peihua Xu

Received: 4 July 2023
Revised: 13 August 2023
Accepted: 16 August 2023
Published: 22 August 2023

1. Introduction

In order to mitigate global warming and limit the rise in global temperature to 2 °C by 2100, as stipulated in the 2015 Paris Agreement, it is necessary to decarbonize the energy sector by utilizing renewable energies as a fundamental strategy. To achieve this objective, the world must shift its thermal energy sources towards renewable sources, including geothermal, solar, and bioenergy. However, despite the suitability of geothermal energy for addressing modern thermal needs, it only accounted for 0.77% of all thermal energy use worldwide in 2021 [1,2], while fossil fuels and firewood accounted for 40% and 49%, respectively [3].

Transitioning to an energy system based on renewable sources and energy efficiency, and away from fossil fuels, could be a game changer for creating a more secure, resilient, low-cost, and sustainable energy future. The utilization of renewable energies has become a crucial factor in meeting the increasing electricity demand [4]. Each nation has its own set of objectives and responsibilities regarding leveraging its potential for renewable energy (RE) sources [5]. The energy sector has witnessed a remarkable achievement for RE sources. The majority of RE is utilized in the power sector and building sector. However, except for the power sector, the share of RE in all other sectors is increasing slowly. Between 2011 and 2021, the share of RE in global electricity generation increased by 8%, with solar and wind power accounting for over 10% of the total electricity produced for the first time in history. The share of RE in electricity generation increased by 7.9% between 2011 and 2021, as shown in Figure 1. Despite this progress, the current adoption rate of RE is insufficient to achieve the net-zero emissions goal by 2050 [4].

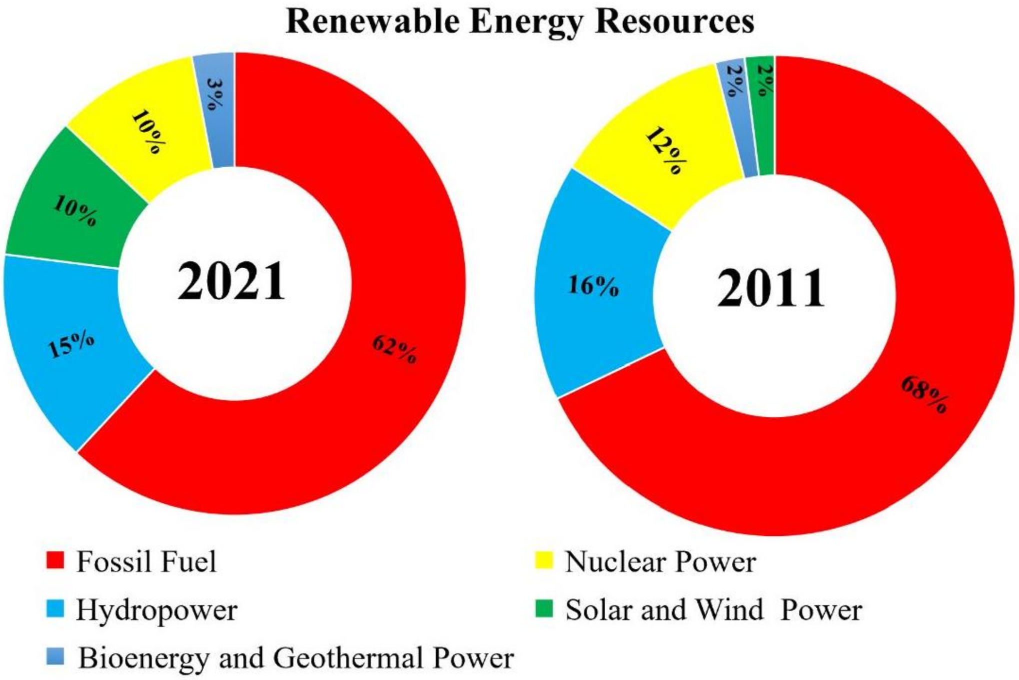

Figure 1. Renewable energy resources worldwide-contribution changes between 2011 and 2021 (Source of Data, [4]).

One reason for the low percentage of geothermal resource usage is the limited availability of high-enthalpy geothermal resources and the high costs and risks associated with developing geothermal fields. Nevertheless, the direct use of geothermal energy, which involves utilizing geothermal resources for meeting thermal needs, such as residential and space heating, horticultural greenhouse warming, and industrial heating, has experienced steady annual growth over the past two-and-a-half decades, with residential and space heating, and bathing and swimming increasing by 8.3% and 6.6%, respectively [1,2]. Including ground-source heat pumps in geothermal energy utilization boosts the direct use of geothermal energy to 1.55% of the total global thermal energy usage [4].

A literature survey reported that numerous studies have been performed to investigate HR geothermal potential using various techniques, which have included: geochemical analysis, major-elements and trace-elements analysis, geothermal gradient analysis, geothermal fluid characterization, gravity and magnetic analysis, structural trend analysis, and geothermal well drilling [6–10]. However, previous studies have not fully mapped prospective zones, which are crucial for understanding and assessing geothermal potential. Conventional geophysical approaches have limitations in identifying geothermal potential in the study areas. Therefore, worldwide researchers have suggested that Remote Sensing (RS) and Geographic Information System (GIS) techniques, including thermal bands on satellite images like Landsat−8 OLI/TIRS, be considered as valuable and cost-effective tools for evaluating geothermal resources. These methods estimate the land surface temperature (LST) and have been employed by researchers to delineate areas with geothermal potential in different geological settings [11–14].

Geothermal energy is harnessed from the Earth's interior, utilizing the heat stored in underground reservoirs as steam and hot water, making it an RE source. Its advantages include its environmentally friendly nature and the minimal space required for exploration and extraction processes. Additionally, geothermal energy has the potential to contribute to the local economy through geo-tourism initiatives [15,16]. Thermal infrared RS is an emerging technique that has proven to be valuable in detecting thermal anomalies within geothermal and volcanic regions. Mapping geothermal anomalies is crucial in identifying target areas for geothermal prospects and the further development of geothermal resource utilization. Infrared RS has emerged as a popular technology for detecting geothermal anomalies on a larger scale in remote areas. RS data enable the effective retrieval of LST, accurately identifying hot spring locations and estimating thermal anomaly distribution characteristics [17,18]. Recent advancements in machine learning (ML) techniques and their application to geology and geoscience have greatly benefited geothermal energy during exploration. The applications of ML techniques to characterizing geothermal exploration processes have led to more efficient and cost-effective research [19,20].

Harrat Rahat is located in the central-western Kingdom of Saudi Arabia and is among the many large volcanic fields dominated by basalt. HR is an excellent example of continental intraplate volcanism. Its exceptional exposure makes it an ideal site for studying the evolution of volcanic flux and composition evolution over time in a continental basalt field [21]. Pre-feasibility studies for low- and medium-temperature resources should be initiated to promote further development. The demand for medium-temperature prospect mapping and diesel power plant substitution using geothermal energy is increasing to meet the electricity needs of rural and remote areas. Low- and medium-temperature resources have various direct and indirect applications that can be developed [5].

The present study aims to evaluate the geothermal potential of the HR volcanic field through the petrophysics data from twenty-one (21) wells and RS data. Subsurface temperature mapping was performed to determine the variation in temperature distribution. The research provides a comprehensive discussion of the various geophysical and geological datasets and their interpretation, highlighting the importance of combining different geophysical methods to understand geothermal systems. Furthermore, supervised machine learning techniques have been applied to predict the temperature from the borehole data. This study has attempted to build a model that connects input vectors/scalars (including temperature and magnetic field) spatially, such as geothermal energy sites around the volcanic region of the HR volcanic field. Machine learning techniques were applied to solve technical problems like the absence of borehole temperature records or inaccuracies in the locations of wells. Researchers around the globe have utilized bottom-hole temperature data from well datasets to create temperature-at-depth maps to identify potential geothermal active zones. Multiple datasets, including geological maps, subsurface borehole temperature distribution maps, and LST maps, were used to determine the distribution of geothermal anomalies. Furthermore, the analysis of LST data using GIS indicated the presence of volcanic activity in the subsurface, which could potentially act as pathways for the flow of heated fluids.

2. Geological Setting and Study Area Description

The current study aims to assess the potential for geothermal reservoirs within the HR volcanic field through geophysical and geological datasets. Integrated research has been carried out to assess the geothermal potential. This study's benefit would be accurately predicting the temperature and finding other sites from the trained data to help predict sites for exploration and drilling operations. The largest volcanic field in Saudi Arabia is the HR volcanic field, which has an area ranging from 50 to 75 km wide (east–west direction) and around 300 km long (north–south direction). Within the Arabian Plate, it is the biggest of the fifteen Harrats or volcanic fields [22–24]. It comprises over 900 volcanic events across an area of over 20,000 km^2 [7,25]. From north to south, it comprises the smaller volcanic fields of Harrat Turrah, Rukhq, Abu Rashid, and Bani Abdullah (Figure 2). Due to the location of the holy city of Al-Madinah, the north part of the HR volcanic field is a highly well-known region, as shown in Figure 2. Seismicity data have been used to explore the ground beneath the lithospheric sequence of the Harrats and Arabian tectonic plate in extensive detail with the help of geological and geophysics data [24,26–28].

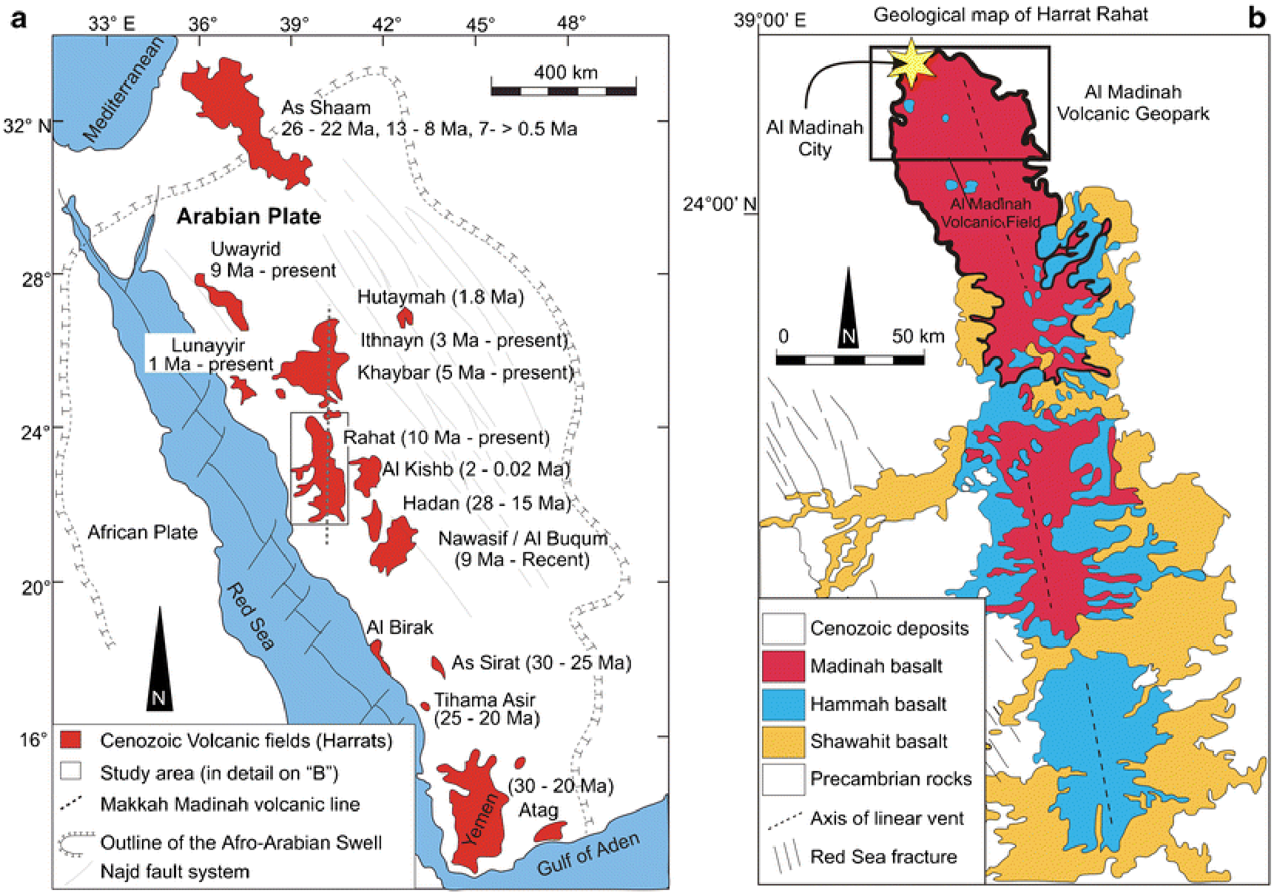

Figure 2. (**a**) The Arabian Peninsula is home to the Cenozoic volcanic fields (Harrats) characterized by vast lava expanses, and their eruption duration range is presented 10 Ma - present. (**b**) Geological map of HR with the main volcanic lithostratigraphy units [22,23].

Due to the expansion of the Red Sea and the Gulf of Aden rifts, the Arabian Plate split apart from the African Plate (30–25 Ma). The better-developed silicic rocks and localized volcanic and plutonic basalt sequences in the western portion of the Arabian Plate provide evidence of Late Cenozoic volcanism [24]. The Arabian Plate has experienced at least 21 eruptions during the last 1500 years; the last one was in Yemen in 1937 [7]. The Afar plume (located at the triple junction of the Gulf of Aden, the Red Sea, and East African rift systems) has been interpreted as being connected to eruptive processes on the Arabian Plate that are older than ten million years. Under the Arabian Plate, the Afar plume moves in a north-side direction. This movement is consistent with the aligned N-S tendency of volcanic fields, such as HR and Harrat Khaybar [29]. The Makkah-Al-Madinah-Nafud Desert (MMN)'s distinctive volcanic line contains HR (Figure 2). Makkah on the southern side, Al-Madinah in the middle, and the Nafud Desert in the north comprise the 600 km long MMN. Numerous experts contend that the Red Sea rifting is not the only source of elevating and tectonics for the MMN [30,31]. The crust of the continent at HR is almost 40 km thick, and the crust and mantle boundary are 60–90 km below the Arabian volcanic fields, while it can extend 150 km on the east side [7,28]. The tectonic features in HR and the nearby Pre-Cambrian settling were initially divided into north-to-east trends at sewed boundaries and thrust faults produced by the Late Proterozoic collision of an island arc, north-to-northeast drifts in the middle vent zone, N-E moment associated with the Cambrian Najd fault phenomena, and E-W trends [29].

Faults and fractures act as pathways for the upward movement of fluids in geothermal fields. This is especially the case in geothermal systems found in extensional and transtensional domains, where both normal and strike-slip faults serve as conduits for fluid flow [32]. The geological structure and dataset play a significant role in finding fluid flow within geothermal systems. Conventionally, geothermal systems have been discovered by drilling near visible geothermal features like fumaroles, hot springs, or known thermal anomalies. Additional methods, such as geological and geophysical data, borehole data, fault mapping, and other tools have been used to understand subsurface geological structures. However, the future growth of geothermal development in Saudi Arabia relies on finding new undiscovered geothermal systems which are not visible on the surface. Subsurface exploration techniques must adapt to rely less on surface geothermal features. It is crucial to incorporate accurate geological and geophysical data to delineate subsurface structural features when analyzing geothermal processes [14,32].

3. Materials and Methods

Bottom hole temperature (BHT) data were collected from twenty-one (21) wells drilled in the HR volcanic field. These data were obtained from Ministry of Environment, Water, and Agriculture (MEWA). Details of the available borehole datasets and well logs cures are described in Table 1. The boundary of the HR volcanic field and well locations is shown in Figure 3. These BHT data were then used to estimate heat flow and temperature distribution at various depths. This study utilized data from the Shuttle Radar Topography Mission (SRTM), obtained from NASA, with a spatial resolution of 30 m, to analyze the HR volcanic field. In addition, Landsat satellite data were employed to calculate LST and NDVI during the summer season for 2000 and 2021. Landsat 5 TM satellite data were used to gather information about the Earth's surface for 2000. The Operational Land Imager (OLI) of the Landsat-8 satellite images acquired in 2021 was utilized to calculate LST and NDVI. Digital image processing methods were employed for said purpose.

Table 1. Details of available borehole dataset and well logs cures.

Well Name	CALP	NGAM	HRD	SHORT	LONG	SP	TEMP	TIME	Th	U	K	DENS	Porosity
RAH-01	✓	✓	✓	✓	✓	✓	✓	×	✓	✓	✓	×	×
RAH-02	✓	✓	✓	✓	✓	✓	✓	✓	✓	✓	✓	✓	✓
RAH-03	✓	✓	✓	✓	✓	✓	✓	✓	✓	✓	✓	✓	✓
RAH-05	✓	✓	✓	✓	✓	✓	✓	×	✓	✓	✓	✓	✓
RAH-06	✓	✓	✓	✓	✓	✓	✓	✓	✓	✓	✓	✓	✓
RAH-07	✓	✓	✓	✓	✓	✓	✓	✓	✓	✓	✓	×	×
RAH-08	✓	✓	✓	✓	✓	✓	✓	×	×	×	×	×	×
RAH-10	✓	✓	✓	✓	✓	✓	✓	×	×	×	×	×	×
RAH-11	✓	✓	✓	✓	✓	✓	✓	×	×	×	×	×	×
RAH-12	✓	✓	✓	✓	✓	✓	✓	×	✓	✓	✓	×	×
RAH-13	✓	✓	✓	✓	✓	✓	✓	✓	✓	✓	✓	×	×
RAH-15	✓	✓	✓	✓	✓	✓	✓	×	✓	✓	✓	×	×

Table 1. *Cont.*

Well Name	CALP	NGAM	HRD	SHORT	LONG	SP	TEMP	TIME	Th	U	K	DENS	Porosity
RAH-16	✓	✓	✓	✓	✓	✓	✓	×	✓	✓	✓	×	×
RAH-17	✓	✓	✓	✓	✓	✓	✓	×	✓	✓	✓	×	×
RAH-19	✓	✓	✓	✓	✓	✓	✓	✓	✓	✓	✓	×	×
RAH-20	✓	✓	✓	✓	✓	✓	✓	✓	✓	✓	✓	×	×
RAH-21	✓	✓	✓	✓	✓	✓	✓	✓	✓	✓	✓	✓	×
RAH-22	✓	✓	✓	✓	✓	✓	✓	×	✓	✓	✓	×	×
RAH-23	✓	×	×	×	×	×	×	×	×	×	×	×	×
RAH-25	✓	✓	✓	✓	✓	✓	✓	✓	✓	✓	✓	×	×
RAH-27	✓	✓	✓	✓	✓	✓	×	×	✓	✓	✓	×	×

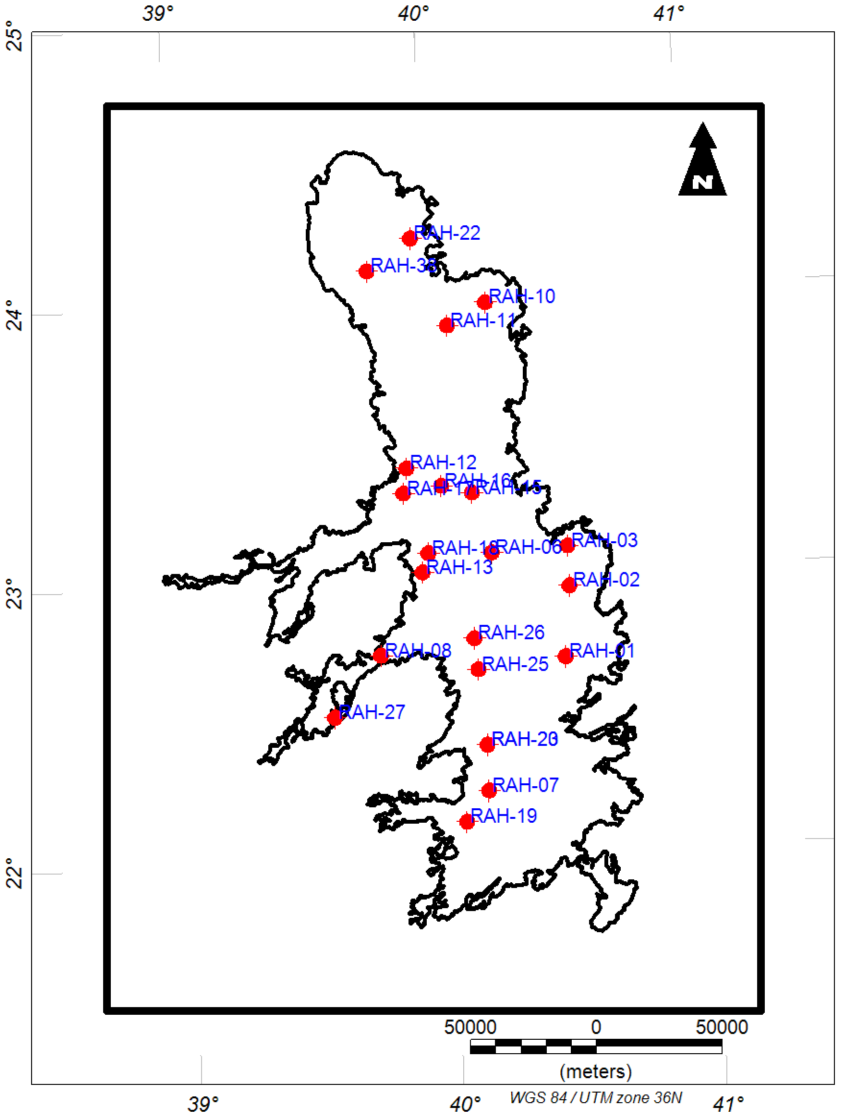

Figure 3. The boundary of the HR volcanic field and well locations.

This study utilized thermal infrared sensor (TIRS) and OLI images from Landsat 5 TM and Landsat 8 for the years 2000 and 2021, respectively. These images were employed for vegetation changes (measured through the NDVI) and LST within the study area. These parameters are known to be indicative of geothermal characteristics, such as the presence of hydrothermal and warm ground on the surface. By analyzing these thermal infrared images, this study aims to provide insights into the geothermal activity and prospecting potential of the HR volcanic field. The Emissions Database for Global Atmospheric Research (EDGAR) dataset was used to develop the CO_2 emission distribution map of the study area.

3.1. Well Logs Analysis

First, we perform a data quality check and select four wells based on their temperature value being less than 50 °C and depth being higher than 450 m. RAH-02, RAH-07, RAH-13, and RAH-17 are used for further well logs analysis to perform machine learning for predicting the temperature. The available log curves for the four selected wells are natural gamma ray (NGAM), self-potential (SP), long normal resistivity (LONG), short normal resistivity (SHRT), high resolution density (HRD), formation density (DENS), porosity, borehole temperature (TEMP), time, thorium (Th), uranium (U), and potassium (K). The graphical display of the well log curve of RAH-13 is shown in Figure 4. The detailed methodology of the work performed based on the curves is described step-by-step in Figure 5.

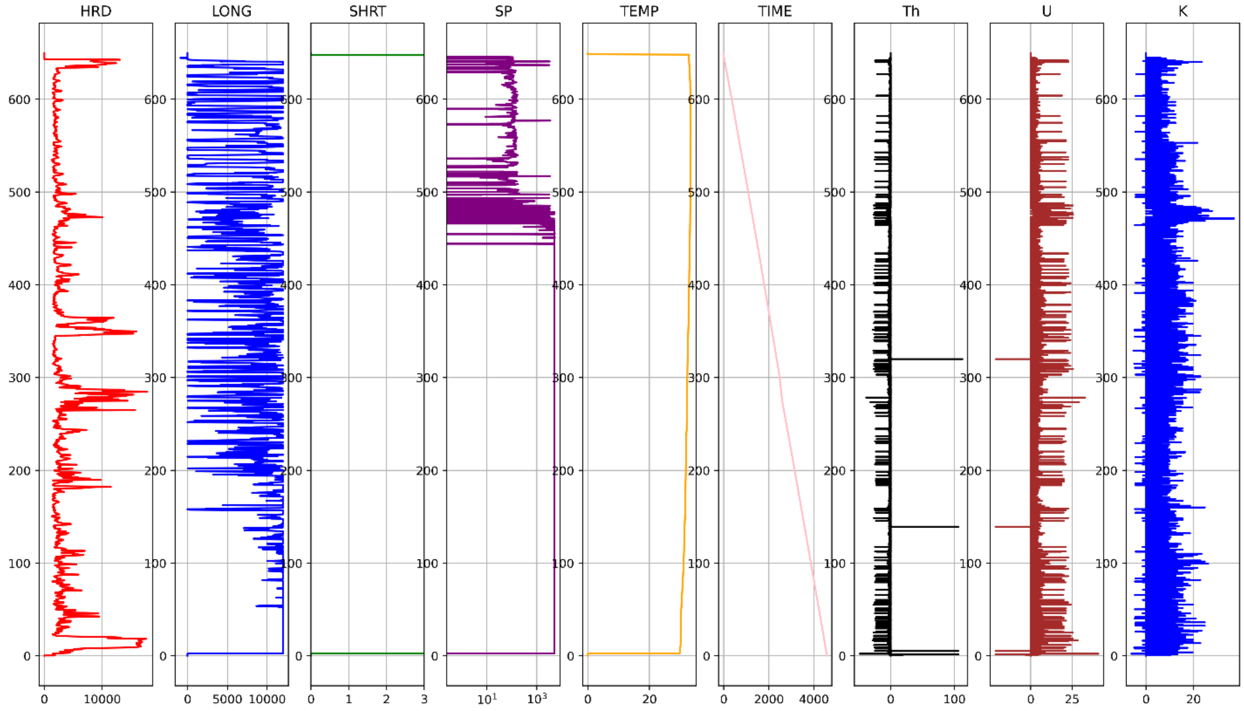

Figure 4. Log curve of RAH-13 well present in HR.

3.1.1. Subsurface Temperature Mapping

The subsurface temperature maps were made with the help of temperature log curves. The subsurface temperature mapping was generated. The reason for making these maps was to know the thermal potential of the subsurface. The temperature mapping was made at depth intervals of initial depth, 50 m, 100 m, and 125 m, encounters in wells.

3.1.2. Heat Production (HP)

GR spectrometry is frequently used in the lab to assess HP [33]. Numerous researchers have used various methods to evaluate HP, including the airborne spectrometry GR approach [34,35] and the GR logging method [36]. When calculating HP as a function of depth, the natural GR log using API (American Petroleum Institute) units is quite helpful [37].

So, for calculating the HP parameter, we employed the GR log. We used Equation (1) to determine the HP.

$$\mathrm{HP}(\mu\mathrm{w/m}^3) = 0.0158\ (\mathrm{GR\ (API)} - 0.8) \tag{1}$$

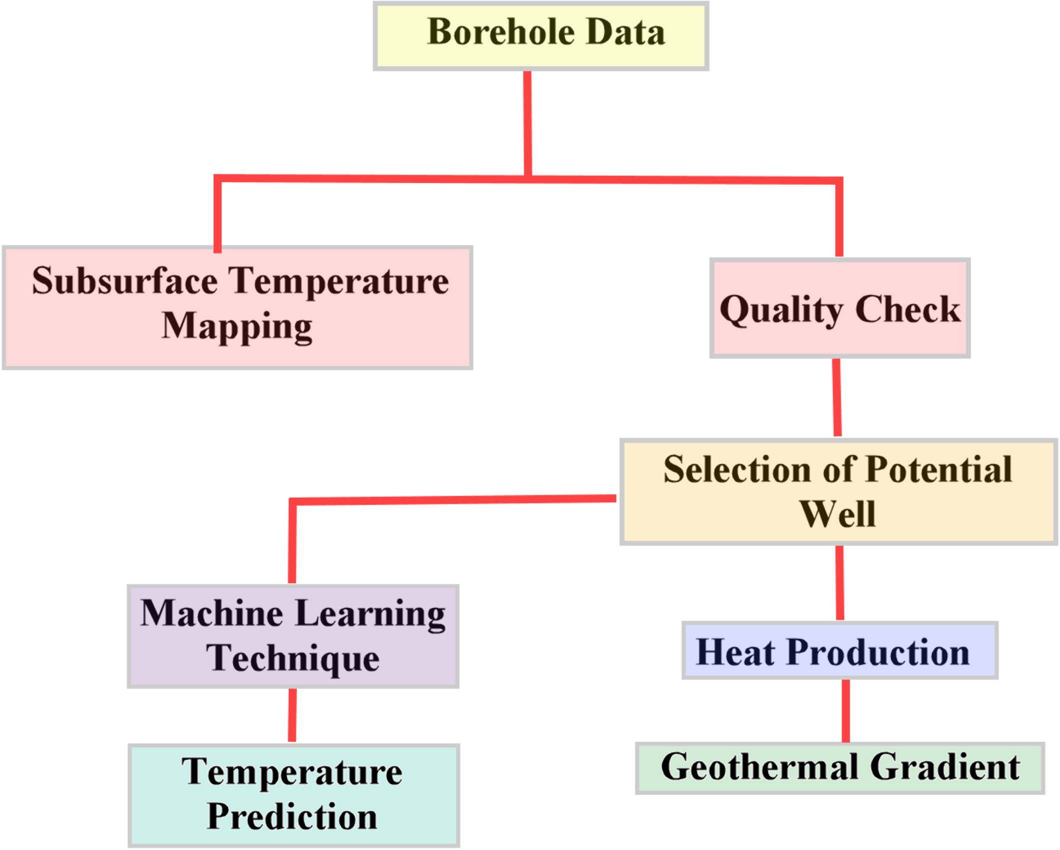

Figure 5. Workflow adopted for well logs analysis.

3.1.3. Geothermal Gradient

A subsurface well reveals a consistent increase in temperature with depth [38]. According to Lashin et al. (2014), the temperature increase is typically expressed as a function of a geothermal gradient (GG) and rises per kilometer of depth. The existence of a radioactive element, which raises temperatures without regard to depth, gradually causes the subsurface temperature to increase. According to Cooper and Cowan (2006) [39], the geothermal gradient can be calculated using Equation (2).

$$GG = \frac{T_{formation} - T_{surface}}{Depth} \tag{2}$$

3.1.4. Temperature Prediction Using Machine Learning

Machine Learning (ML) has arisen as a novel method for solving technical issues, such as missing wellbore logs or errors in observed logs [20]. Supervised machine learning is the fundamental method of ML, which means that once both the data input and the associated identify are known and supplied to the technique, its algorithms build a model to connect the input (or feature) vector to a conforming label or objective vector using training information [40]. The component of the regression technique, called log curve prediction or correction, is employed to forecast discrete values [20].

Unattainable or insufficient observations were eliminated from the chosen log curve before training with the selected model. The splitting of data over three standard deviations (SD) from the data average was considered to be an outlier. The outlier was removed with the SD filter's help, and the SD result is shown in Figure 6. The pair plot with and without removing the outlier are shown in Figures S1 and S2, respectively.

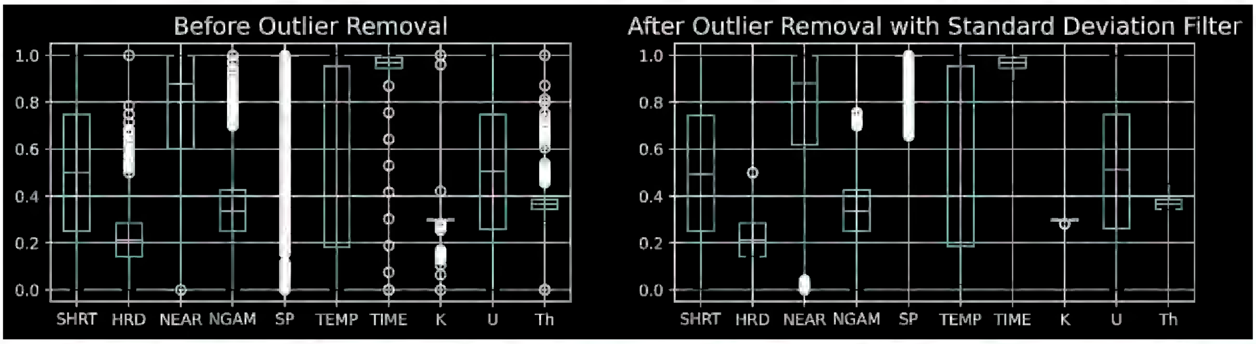

Figure 6. Before and after the removal of the outlier with the standard deviation filter of RAH-13.

Several strategies were used to identify the missing numbers, comprehend the data distribution, and visualize the available data after the data were imported into Excel. Python's Panda's Library was employed for this intended purpose. The exploratory data analysis (EDA) method was used to manage the data. Exploratory research is the evaluation procedure for conducting the first analysis of the provided data to investigate hypotheses, discover abnormalities, identify trends, and check assumptions with the aid of visualizations [41]. We evaluated the data at this step to see if further processing or purifying was required. The import of CSV into Python, a bar plot (Figure 7) that aids in assessing the accuracy of the data, was created using the 'missingno' package. The Seaborn module for Python was utilized to examine the multi-factor variation in the information [42]. We plotted a pair plot that provided essential details regarding the data quality. It provided the data's dispersion type.

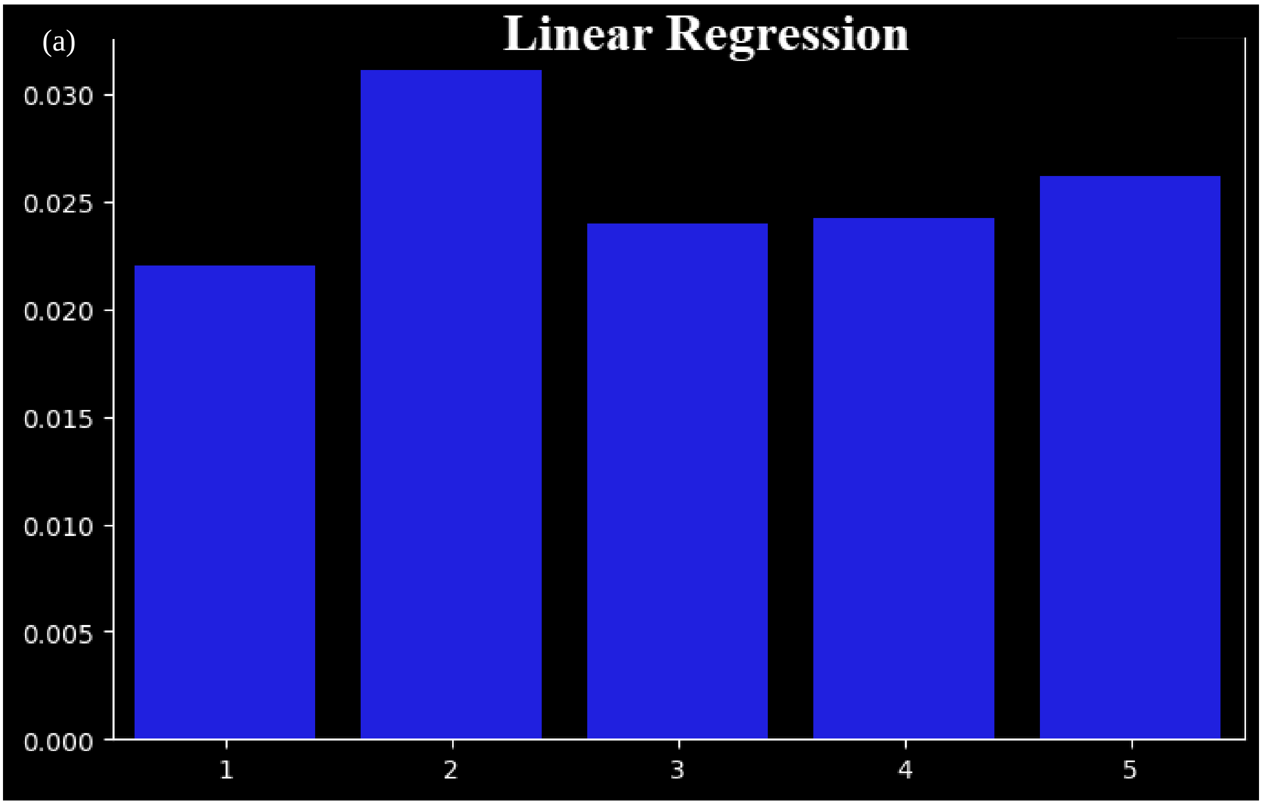

Figure 7. *Cont.*

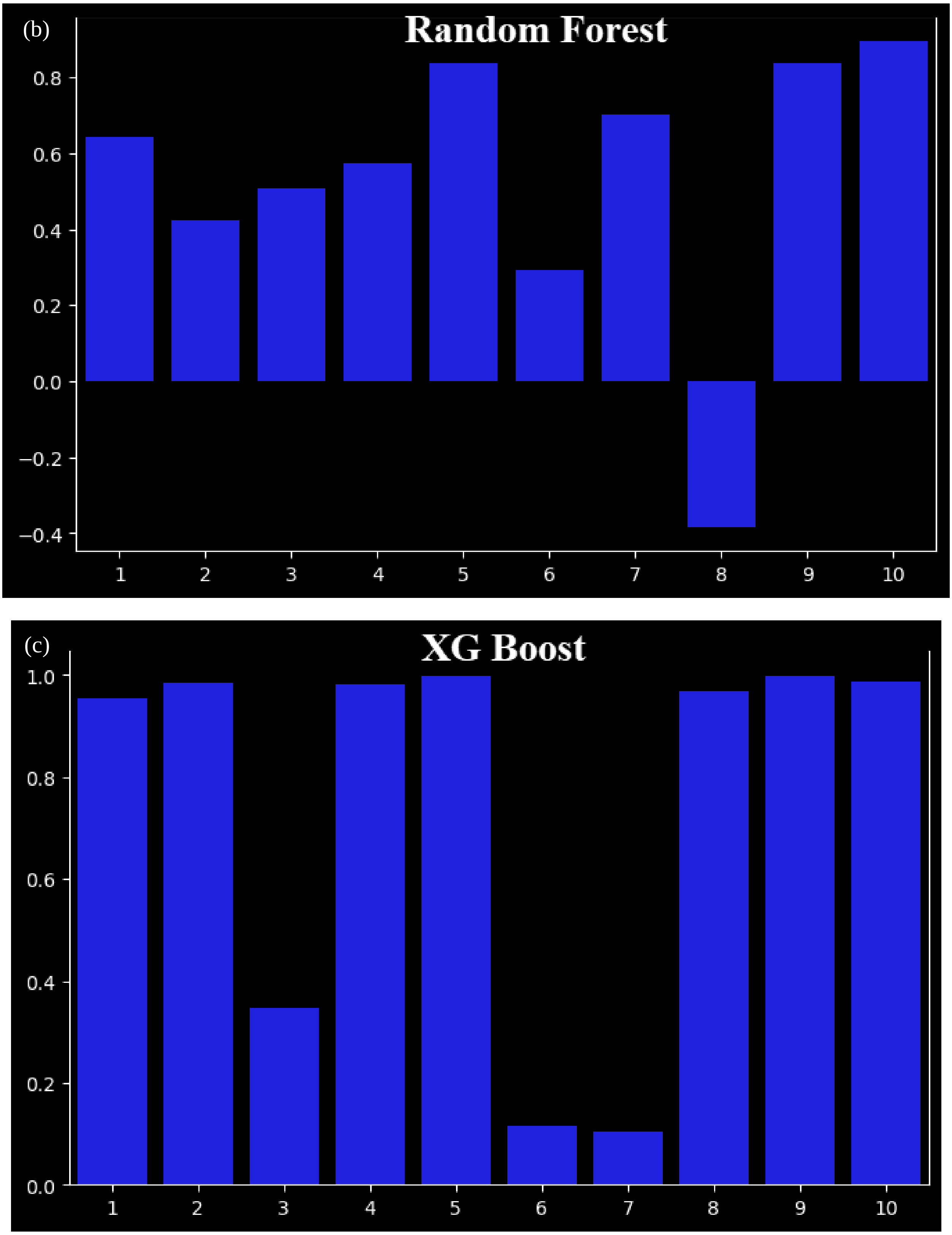

Figure 7. Bar plot for cross-validation score of (**a**) linear regression, (**b**) random forest, and (**c**) XGBoost model for temperature prediction.

Temperature logging refers to the subsurface temperature measure in centigrade for a geothermal formation analysis. We calculated the temperature log data by constructing a predictive model using regression techniques. Linear regression (LR) is the name of the model where a dependent variable, (y), is related to a single independent variable, (x). Linear regression is a statistical tool that estimates the linear connection between a supported variable and one or more independent features [43,44]. Regression modeling is used to assess the connection among many variables. The corresponding characteristics between the two parameters are unaffected by the data linkage. This model needs a goal position to be forecasted and a variable that closely connects to the objective point. The parameter was chosen using a correlation matrix, and the chances were scaled from 1 to 1 (Figure 7). The training and prediction stages comprised the supervised-learning workflow [45]. It was observed that temperature, with a value of 0.98, closely corresponds to the temperature curve values. The model was trained using 80% of the points in Euclidian space and tested using the remaining 20% of the data points. The evaluation of performance matrices was used to verify the precision of the created framework. There are numerous evaluation metrics for distinct models. The root mean squared error (RMSE), R^2 scores, the correlation between testing data and predicted data, and a graph of actual values vs. predicted ones, are common performance indicators for most algorithms.

3.2. Magnetic Data

Regional aeromagnetic surveys were conducted over the Precambrian rocks of the Arabian Shield during the years 1962, 1965–1966, and subsequently in smaller areas between 1976 and early 1983. The purpose of these surveys was to support mineral prospecting activities in the region. The surveys employed different specifications and techniques depending on the time and area being surveyed.

The initial surveys in 1962 and the comprehensive survey in 1965–1966 utilized terrain clearances of 150 m and 300 m, respectively. The line spacing varied between 500 m and 2000 m, with an approximate spacing of 800 m. Analog recording methods were used during these surveys.

To complete the coverage of the Arabian Shield, additional surveys were conducted in smaller areas, including the volcanic areas known as Harrats, between 1976 and early 1983. These surveys had a line spacing of 2500 m and a terrain clearance of 300 m. In 1976, a survey commissioned by the Saudi–Sudanese Commission focused on the central Red Sea region.

The Phanerozoic rocks, which represent a more recent geological period, were surveyed separately in 1982 and 1983. These surveys employed digital data recording methods and had a terrain clearance of 120 m and a line spacing of 2000 m.

These aeromagnetic surveys were instrumental in gathering information about the magnetic properties of the rocks in the Arabian Shield and the surrounding areas. The data obtained from these surveys can be analyzed to identify potential mineral deposits and geological structures, aiding in mineral prospecting and exploration efforts [46].

Georgel et al. (1990) [46] digitized the early analog data and produced TMI (total magnetic intensity) and RTP (reduced-to-pole) maps in which the data were continued upward to 800 m above ground level. These maps yielded useful information on the regional variations in the magnetic anomaly field, although they tend to lack fine detail. Hase (1970) [47] analyzed the shield's magnetic data, and Johnson and Vranas (1992) [48] conducted an overall analysis of the magnetic patterns in the shield. The cover rock survey data were analyzed at a regional scale by Phoenix Corporation (1985) [49], and locally, the data were analyzed in greater detail (e.g., [50,51]).

The aeromagnetic data were obtained from the Saudi Geological Survey (SGS). An early interpretation of the magnetic data over the Red Sea was provided by [52]. The CET Grid Analysis contains tools for texture analysis, phase analysis, and structure detection. These algorithms are useful for grid texture analysis, lineament detection, edge detection, and threshold detection. More details on the CET can be found in [53–57].

3.3. LST and NDVI and CO_2 Emissions

Conventional surface exploration methods for characterizing potential geothermal areas involve time-consuming and costly field surveys and the gathering of local knowledge through literature surveys. However, these methods are unreliable for inaccessible or remote geothermal areas. To address this issue, this study explored the cost-effectiveness and efficacy of satellite RS in providing an initial land surface characterization for comprehensive geothermal exploration. Surface thermal anomalies associated with geothermal features were delineated [15,18,58,59]. RS and GIS approaches were integrated to map geothermal manifestations and evaluate potential geothermal zones. The mapping process utilized data from Landsat 8 OLI. The utilization of GIS and RS in geothermal exploration proved to be crucial, as these tools offer a more powerful and cost-effective appraisal of geothermal resources [11,60].

The measurement of LST plays a vital role in identifying potential locations for hot springs sites. Landsat satellite images can estimate the surface temperature for the entire study area [13]. The LST derived from RS image inversion was utilized for quantitative analysis, enabling the detection of geothermal anomaly zones to mitigate the impact of solar radiation on the land surface [61]. The collection of LST data offered valuable insights into the distribution and characteristics of geothermal reservoirs and subsurface areas containing hot rocks or fluids suitable for geothermal energy production [61,62].

In this study, 100 different sample locations within the study area were selected to obtain LST and NDVI data within the study area. These sample points, representing the collection sites for LST and NDVI measurements, are depicted in Figure 8, with orange indicating the sample points and black squares representing the boundary of the area under study. The NDVI was calculated using the near-infrared and red bands of the Landsat satellite, as described in Equation (3) [12].

$$\mathrm{NDVI} = \mathrm{NIR} - \mathrm{RED}/\mathrm{NIR} + \mathrm{RED} \tag{3}$$

where NIR is near-infrared and RED is red reflectance.

The values of NDVI and LST were then extracted for the observed years, namely, 2000 and 2021. The relationship between LST and NDVI was determined using Pearson's correlation coefficient approach.

The EDGAR dataset was used to develop the CO_2 emission map over the study field. The prime objective of EDGAR is to provide scientists and policymakers with information on the evolution of emission inventories for all countries worldwide over time. It also offers the scientific community grid maps at a resolution of $0.1 \times 0.1°$, illustrating the sources of emissions [63]. It has become evident that a strong correlation exists between active tectonic regions and unusual emissions of CO_2 from the Earth's crust. Their high permeability characterizes faults and fractures and serves as preferential pathways for the upward migration and release of deep-seated gases into reservoirs or the atmosphere. Indeed, present-day volcanoes release relatively very small quantities of CO_2 compared to land-use changes [64,65]. An increase in geochemical parameters, specifically the LST as well as CO_2 emission within the volcanic active area, were observed [66].

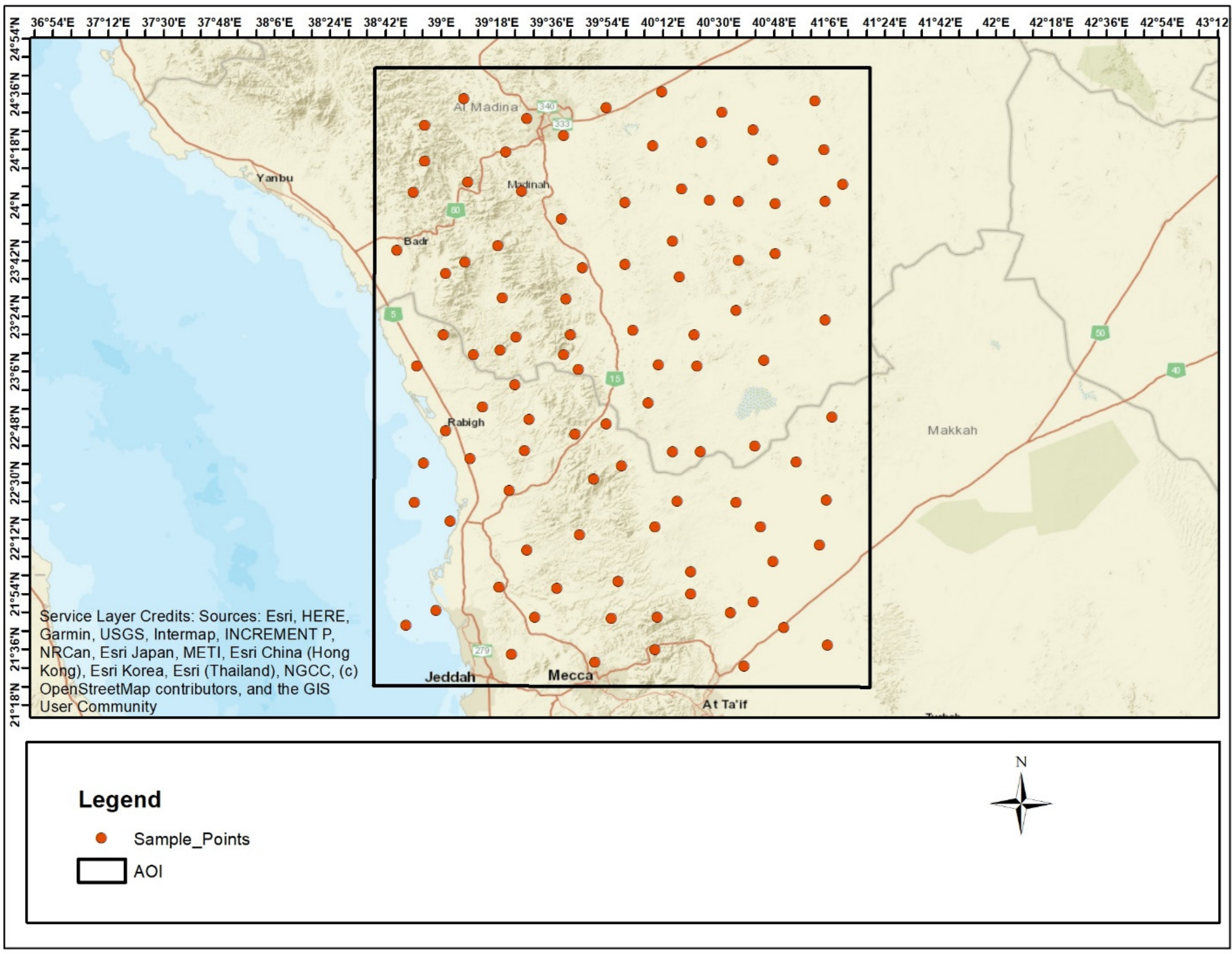

Figure 8. These sample points represent the LST and NDVI measurement collection sites in the HR volcanic field.

4. Results and Discussions

Saudi Arabia has a wealth of geothermal energy resources. Still, little research has been performed to assess their potentials, notably in the west side of the country near the Red Sea coast, where volcanic fields and hot springs are present [6]. It has been proposed that the volcanic fields in Rahat and Khaybar have geothermal potential. Additionally, the largest potential of geothermal zones is found on the west side, sideways in the direction of the Red Sea, corresponding to the geothermal resources record recognized for Saudi Arabia. Moreover, Rehman and Shash (2005) [67] evaluated the scientific research on geothermal potential and concluded that little geothermal phenomena were currently taking place at the existing geothermal features (such as volcanic fields and hot springs). Hussein et al. (2013) [68] and Lashin et al. (2020) [9] argued that, according to research on the geothermal characteristics of Saudi Arabia, these volcanoes' highly intensive explosive volumes present viable opportunities for constructing geothermal energy plants. Geothermal energy sources with temperatures of up to 150 °C and 300 °C may be found in the indicated geological formations. Because of the lack of deep drilling, there are various doubts regarding the potential. As a result, Saudi Arabia's geothermal resources are sufficient for use on a commercial basis.

4.1. Well Logs Interpretation

A statistical analysis of the temperature logs confirms that RAH-02, 7, 13, and 17 wells have geothermal potential. The maximum temperature range of the wells is approximately 50 degrees Celsius, and the depth of these wells is greater than 450 m. The potential geothermal wells are shown in red, and the remaining wells are highlighted in blue, as shown in Figure 9.

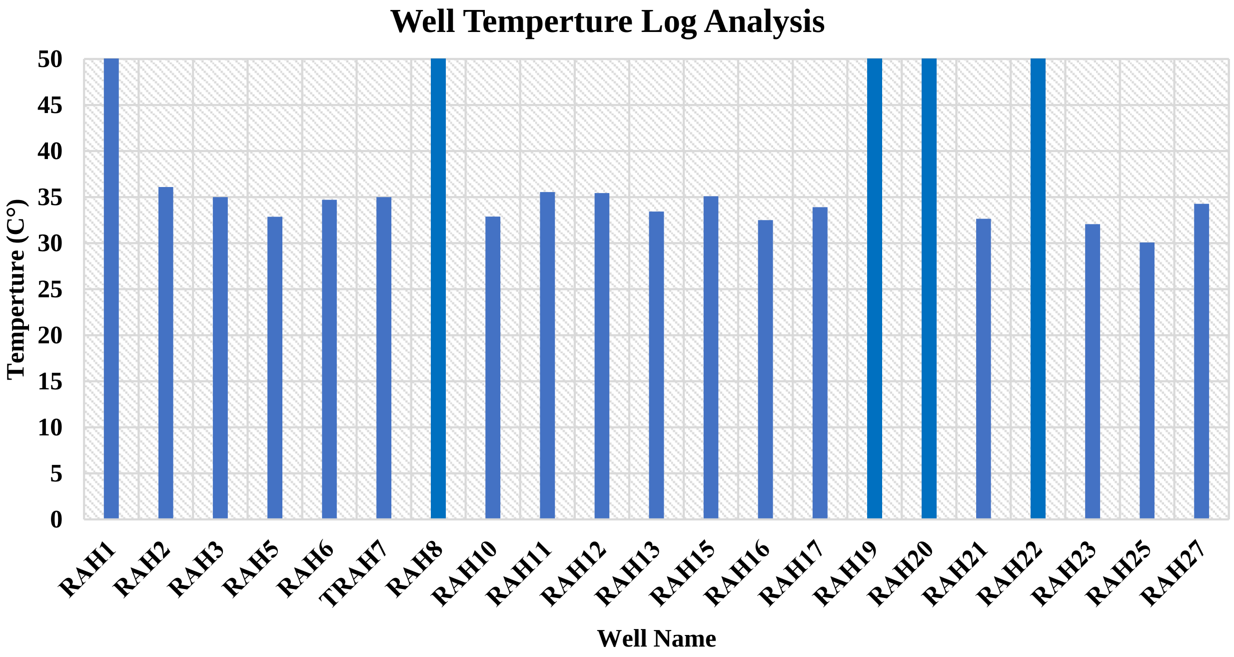

Figure 9. Well logs temperature graphical presentation, which shows the names of the wells plotted on the *X*-axis and the temperature on the *Y*-axis.

4.1.1. Subsurface Temperature Mapping

Subsurface temperature mapping was performed to assess the temperature variation with respect to depth. Temperature maps were developed at depths of 10 m, 50 m, 100 m, 125 m, and 150 m, as shown in Figure 10. The range of temperature varies from 0 to 40 °C. It can be observed that the south portion of the map shows geothermal potential because the highest temperature is encountered in that area.

4.1.2. Heat Production and Geothermal Gradient

The temperature log curves, which show a rising consistency with the logs at depth, demonstrate that various elements, including timely response, position, depth, and geology, can generate temperature differences. Using a probe to determine the temperature distribution among numerous logs is also feasible due to variations in speed, temperature inclination, and duration [69,70]. All the wells had their results evaluated based on the available well data. The optimal outcome revealed that the higher typical temperatures for borehole RAH 02, 07, 13 are less than 50 C °. Due to the significant fluctuations in the drillings, the calculated temperature accurately reflects the formation temperature. Usually, a great radioactive substance is involved in the measurement formation of the GR log. The GR log was used in the calculation of HP. The HP curve shows the variation within the total log profile that indicates there is the presence of a geothermal anomaly below ground. The well logs are illustrated in Figures 11–14, for both the heat production and geothermal gradient for wells RAH-02, RAH-07, RAH-13 and RAH-17, respectively. The depth between 135 and 142 m shows the presence of a geothermal body, and the spike in HP and GG are a clear indication of a geothermal anomaly in the RAH-08 well. Geothermal resources are present in the subsurface, according to the results of GG and HP.

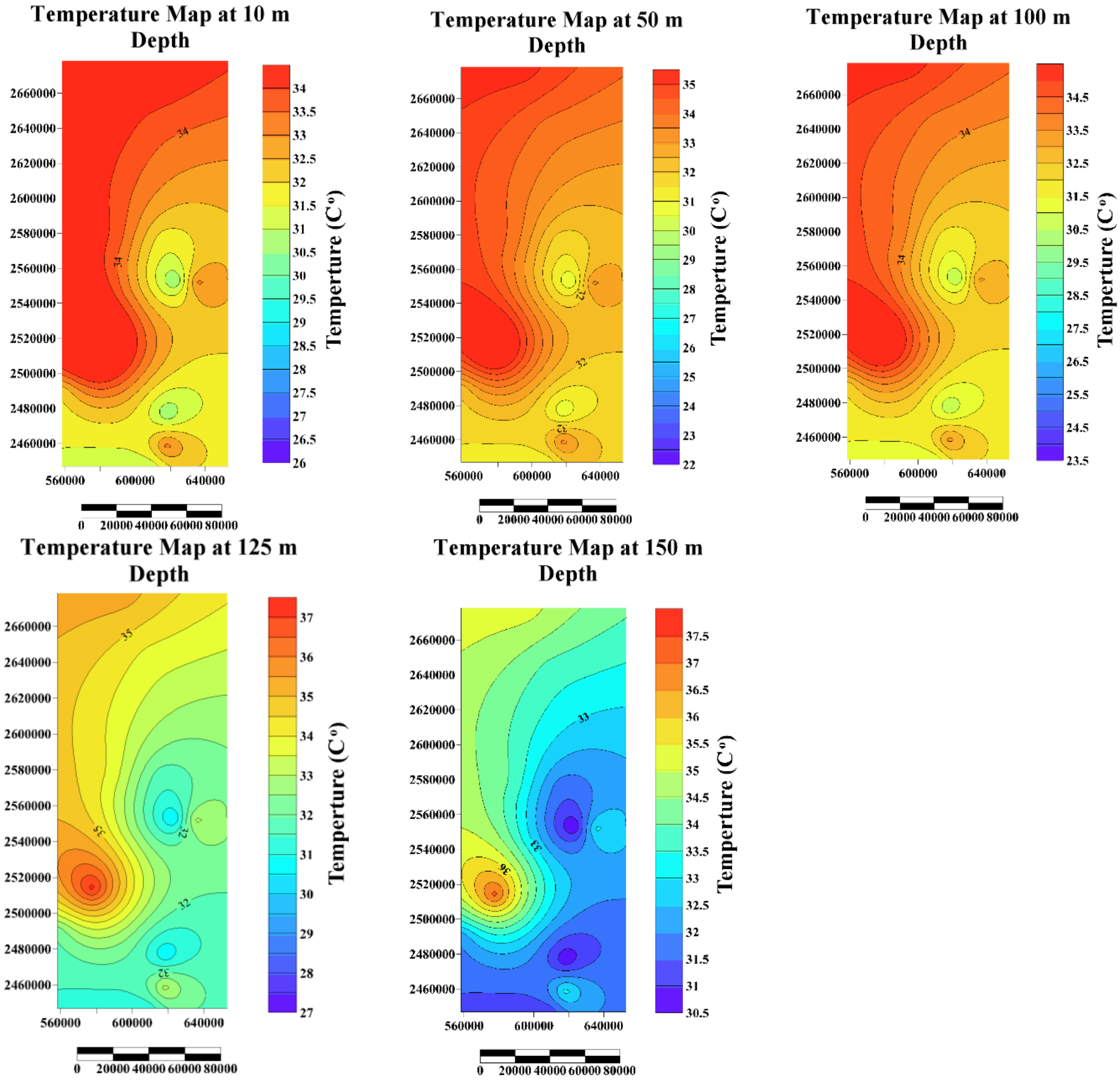

Figure 10. Subsurface temperature maps were developed at 10 m, 50 m, 100 m, 125 m, and 150 m.

4.1.3. Temperature Prediction

For the evaluation, we adopted the corrected temperature data to estimate the linear regression, random forest, and XG Boost alongside the temperature model. Jordan et al. (2016) [71] described the anticipated subsurface temperatures (from the actual temperature) across the depth. Up to four wells' worth of forecasted temperature data are accessible, each with the highest forecasts at various depths. Using a linear regression model, we interpolated the temperature-profile estimations for the real temperatures (in the temperature-profile dataset). The mean absolute errors of the linear regression, random forest, XG Boost, and the actual temperature were determined for the four boreholes after the findings were analyzed. A summary of the ML algorithm results that were applied to the well data is shown in Table 2.

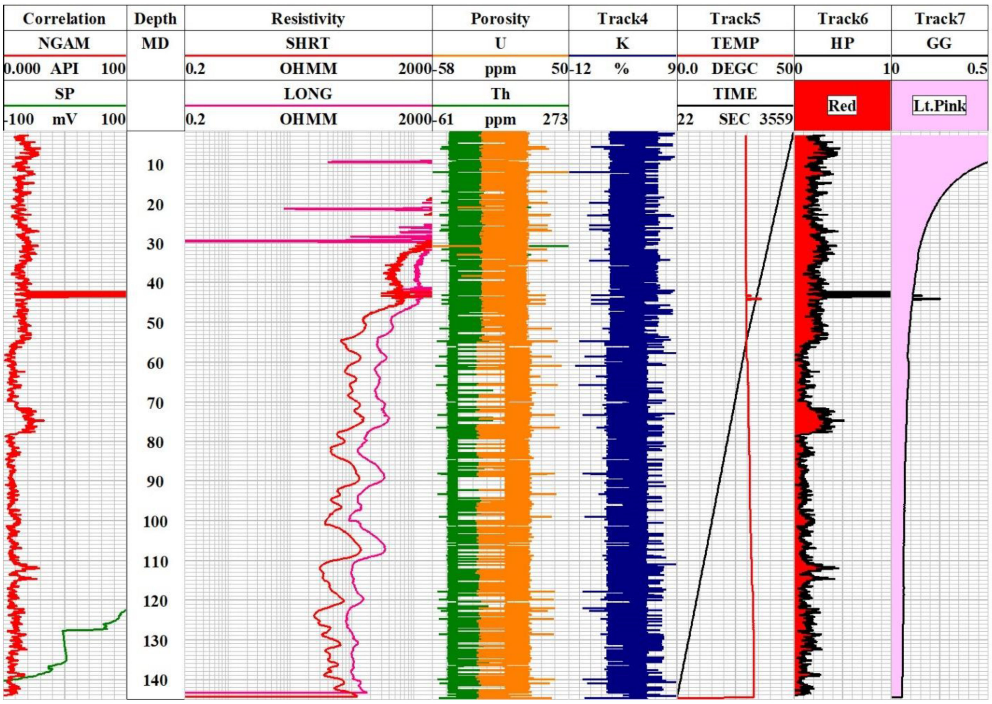

Figure 11. Calculation of HP and GG for the RAH-02 well. The depth is between 0 m and 145 m. The higher the gamma ray log is means the HP is higher and indicates a potential source.

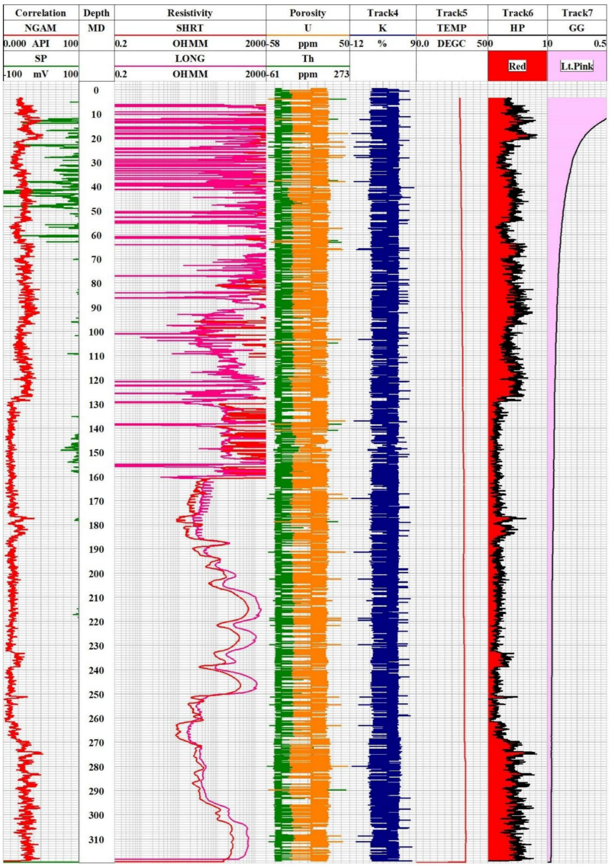

Figure 12. Calculation of HP and GG for the RAH-07 well. The trend of NGAM and HP follow the same pattern; the higher the values of NGAM are, the higher HP is observed.

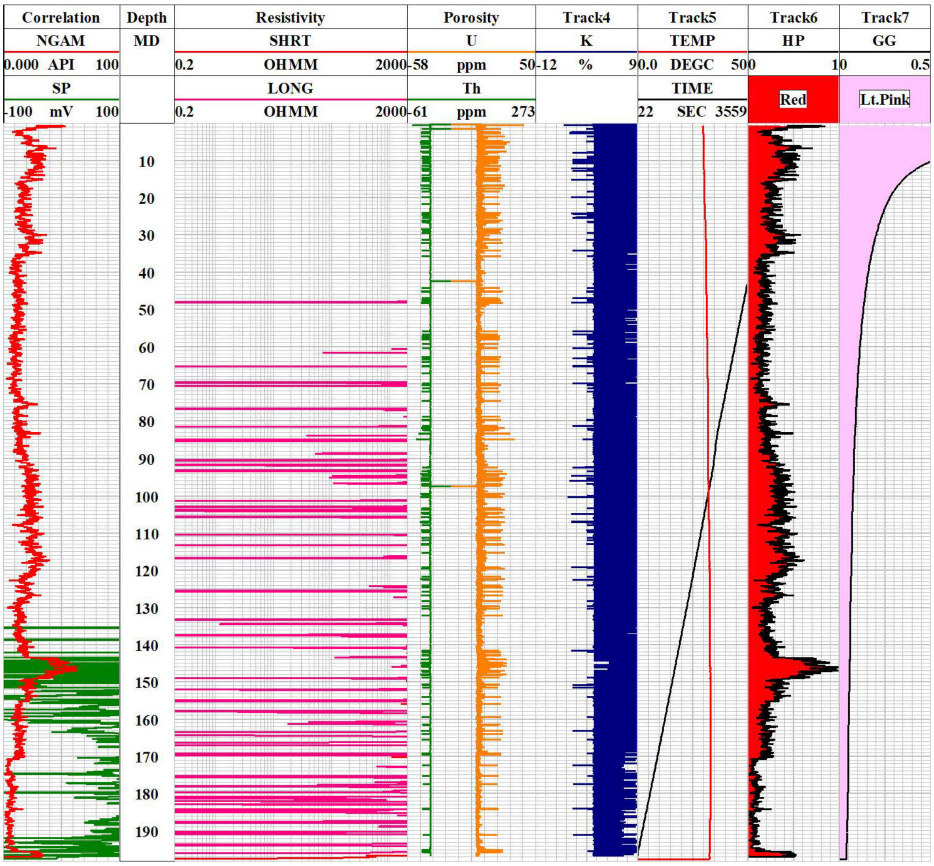

Figure 13. All log curves are available for calculating HP and GG for the RAH-13 well. The maximum HP of this well was observed between depth of a 140 and 160 m. At that depth, higher values of HP were observed.

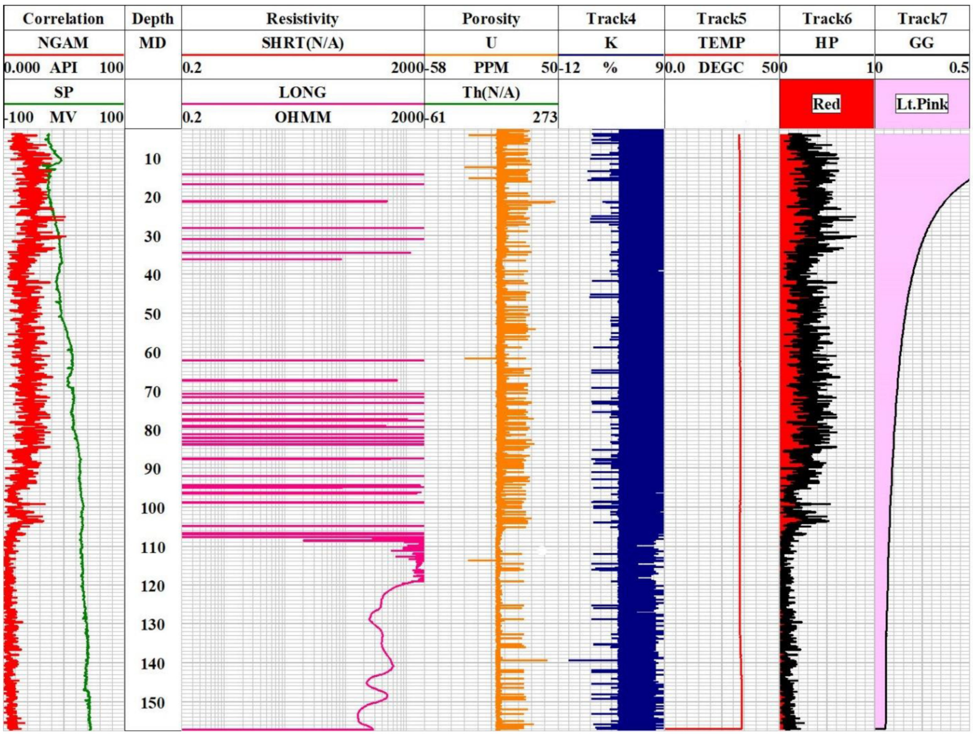

Figure 14. Estimation of HP and GG for the RAH-17 well.

Table 2. A summary of ML algorithm results applied to the well data.

Well Name	Machine Algorithms	Training R^2 Score	Testing R^2 Score	Adjusted R^2	Mean Absolute Error
RAH-02	**Linear Regression**	0.749	0.663	0.661	0.995
	Random Forest	0.999	0.999	0.118	0.010
	XG Boost	0.999	0.997	0.997	0.014
RAH-07	**Linear Regression**	0.259	0.231	0.229	1.185
	Random Forest	0.999	0.993	0.261	0.015
	XG Boost	0.999	0.990	0.997	0.012
RAH-13	**Linear Regression**	0.540	0.561	0.559	0.628
	Random Forest	0.998	0.998	0.291	0.008
	XG Boost	0.999	0.999	0.999	0.007
RAH-17	**Linear Regression**	0.445	0.409	0.405	1.110
	Random Forest	0.999	0.996	0.091	0.031
	XG Boost	0.999	0.999	0.999	0.015

The residuals plot is frequently used to examine the variation in the regression error. A linear regression approach is typically adequate for the data if the points have an even distribution across the horizontal axis; alternatively, a nonlinear model is preferable. Figures 15 and 16 below show the residual cross-plot generated based on XG Boost algorithms. The training data are shown by the green color, and the predicted datasets are shown by the blue color. The RAH-02, 07, 13, and 17 wells show the best results for temperature prediction (Figure 16).

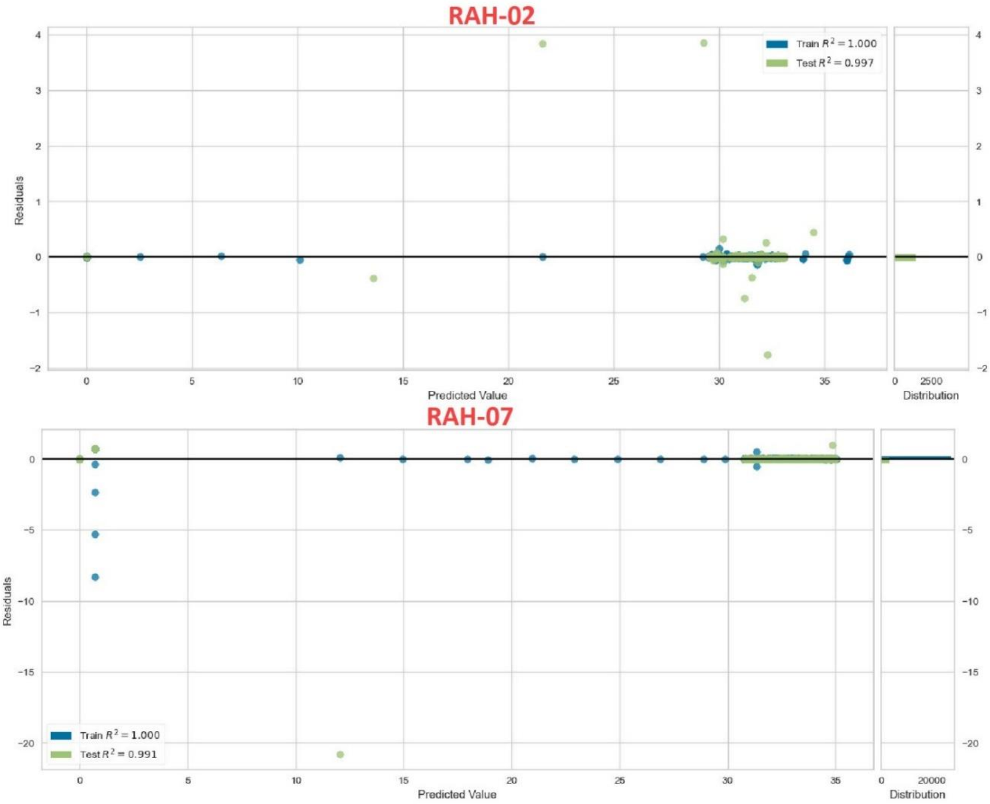

Figure 15. Predicted vs. residual cross plot of the RAH-02 and RAH-07 wells. The green color shows the training point, and the blue color shows the testing point. The residual plot is generated based on the XG Boost algorithm.

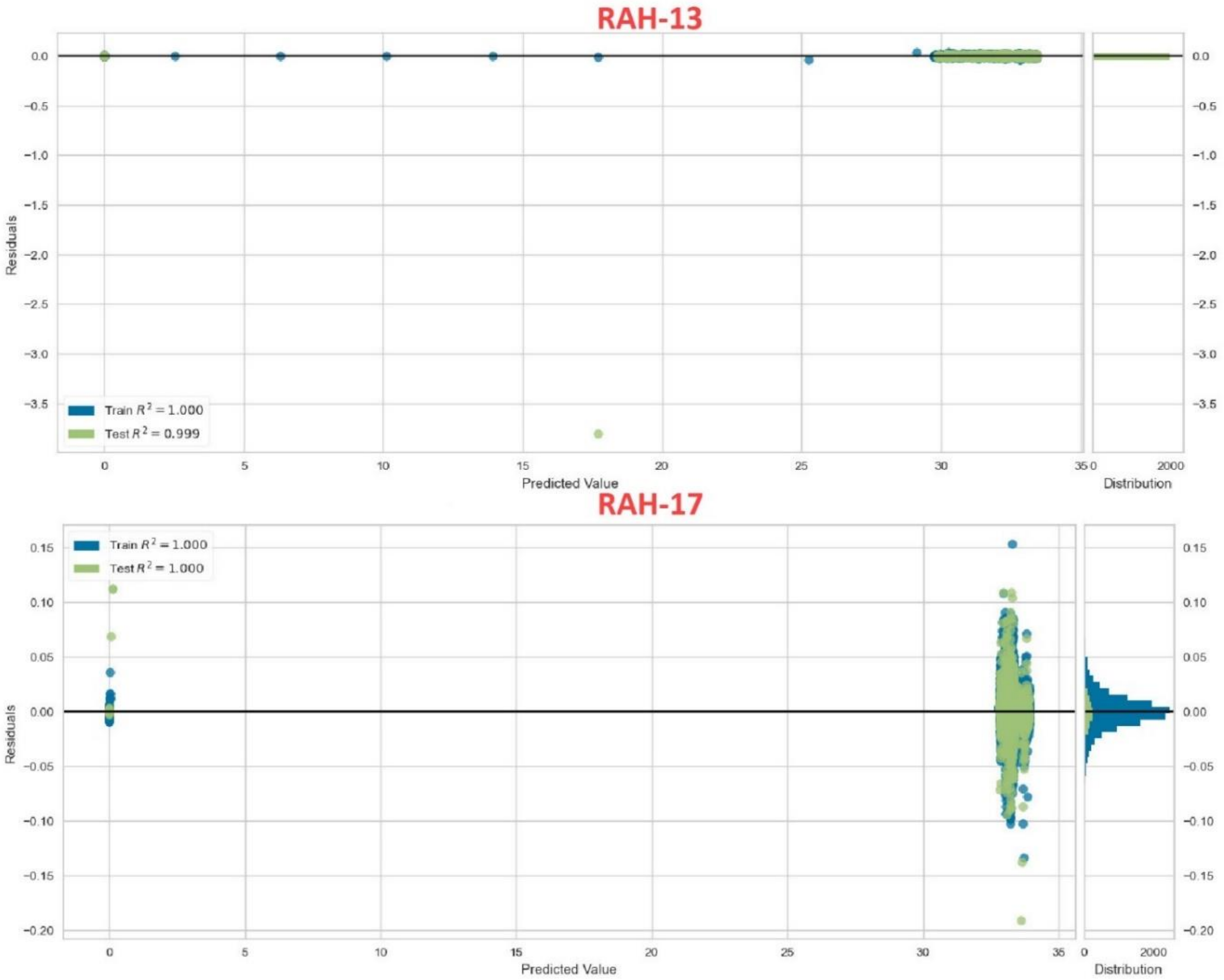

Figure 16. Predicted vs. residual cross plot of the RAH-13 and 17 wells. The green color shows the training point, and the blue color shows the testing point. The residual plot is generated based on the XG Boost algorithm. The black line represents the zero values in the graph; the RAH-13 and RAH -17 give the best results with the XG Boost techniques.

4.1.4. Predicted Temperature

On the basis of all the algorithms, the XG Boost gave the best result for training and testing. So, we used XG Boost for the prediction of the temperature curve. Figures 17–20 are the predicted vs. actual temperature for the RAH-02, 07, 13, and 17 wells, respectively. The predicted temperature is shown in purple, and the true temperature is shown in green. The scattered points show the high-temperature values, which are an indication of a geothermal reservoir.

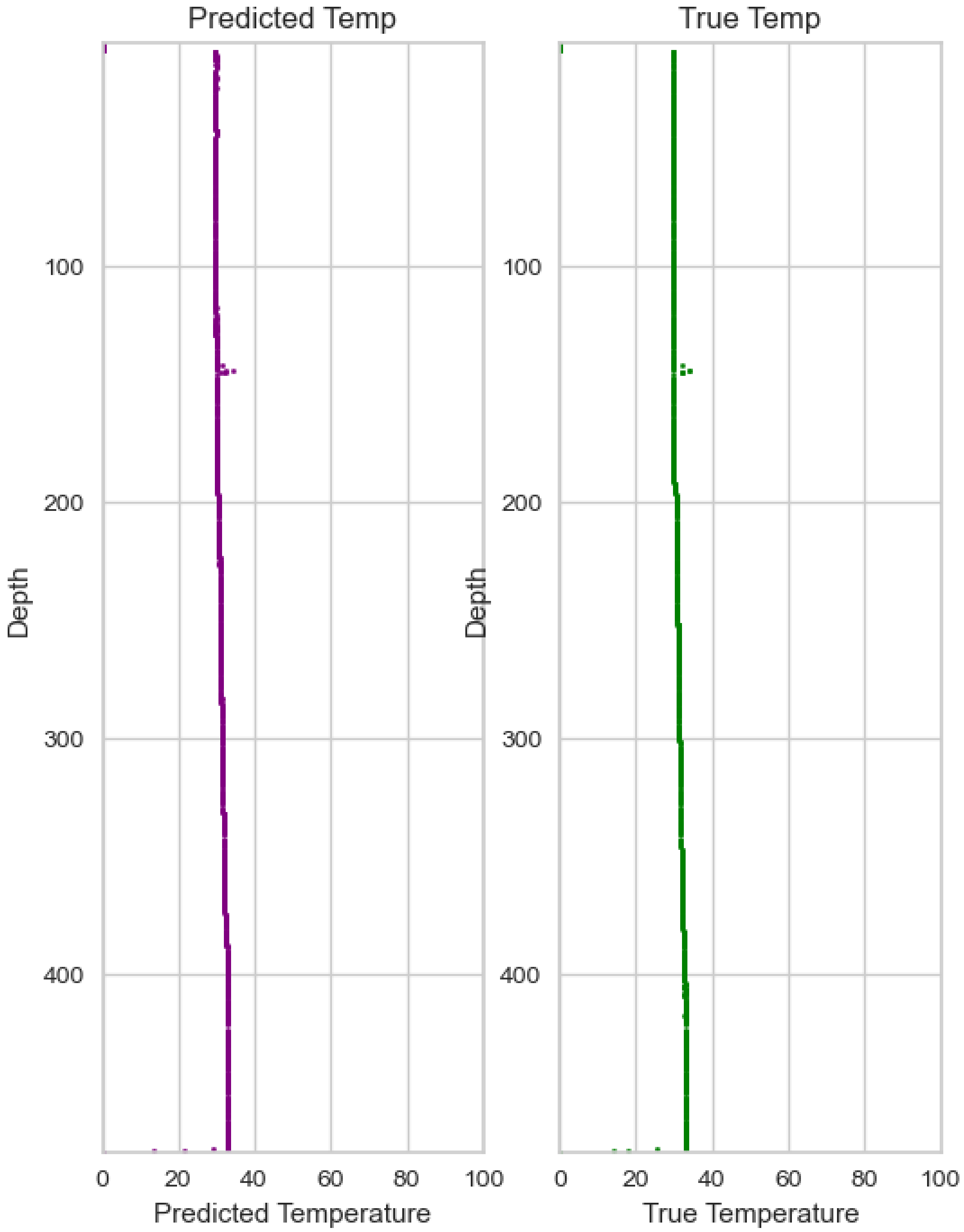

Figure 17. Predicted vs. actual temperature of RAH-02 well based on XG Boost algorithms.

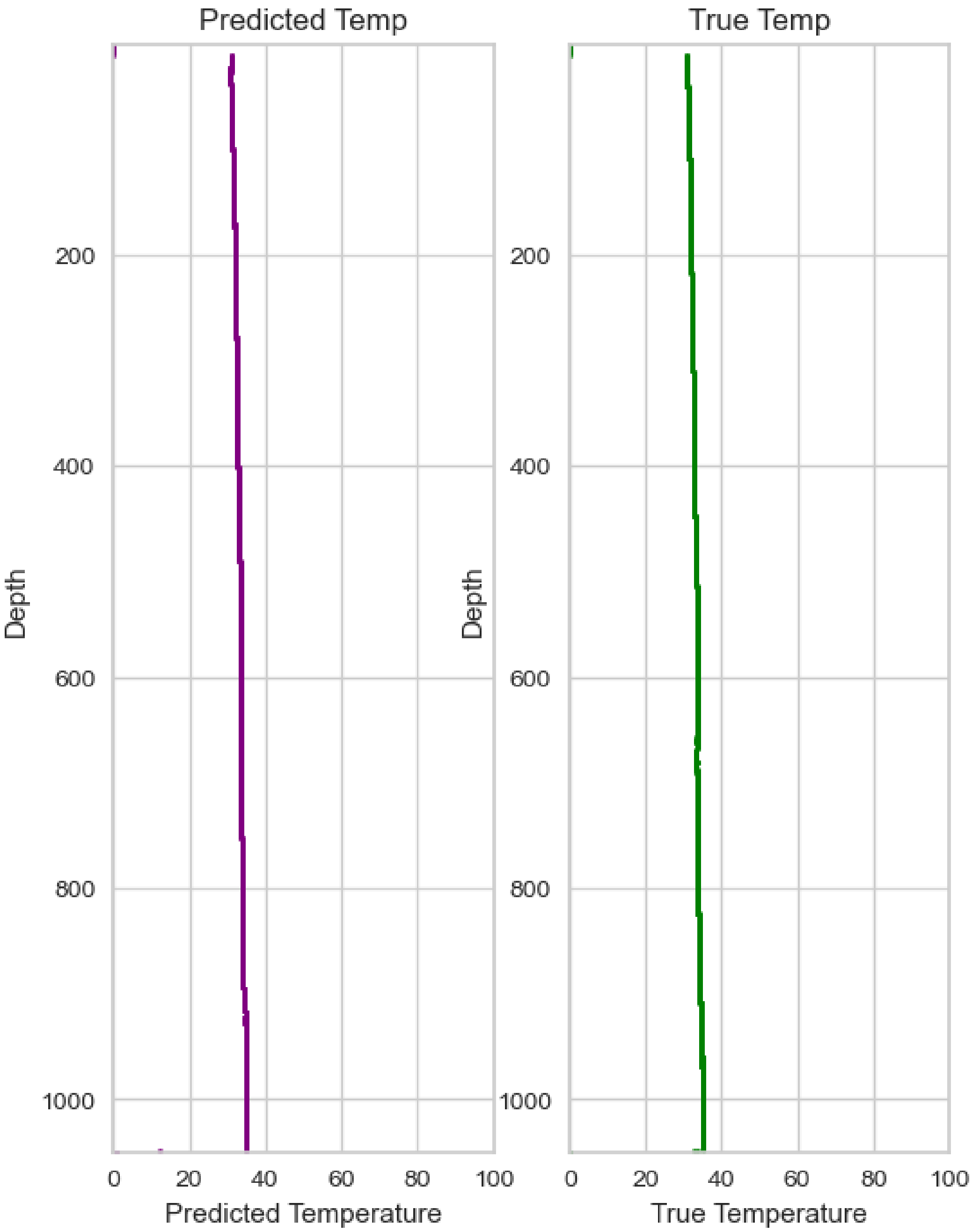

Figure 18. Predicted vs. actual temperature of RAH-07 well based on XG Boost algorithms.

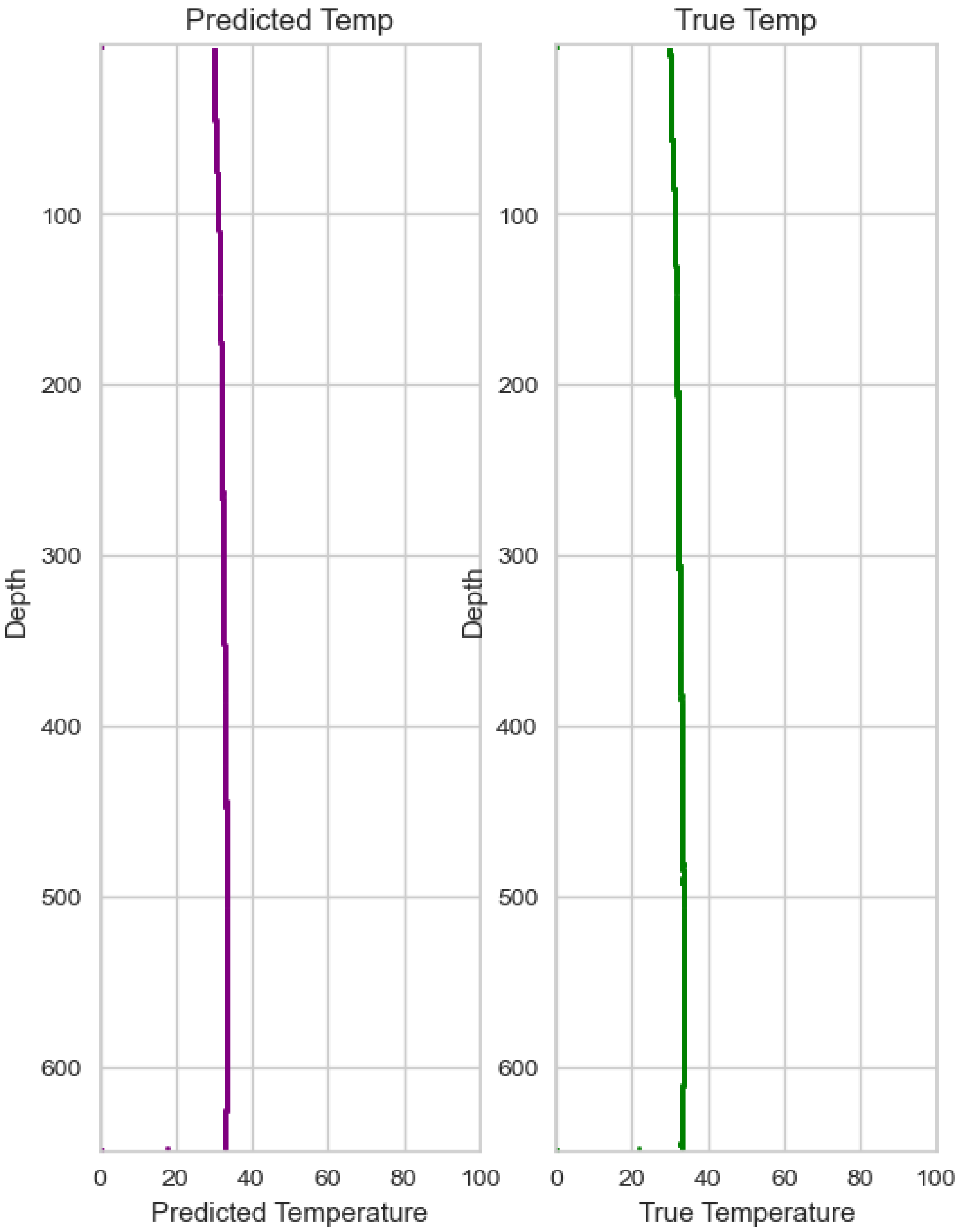

Figure 19. Predicted vs. actual temperature of RAH-13 well based on XG Boost algorithms.

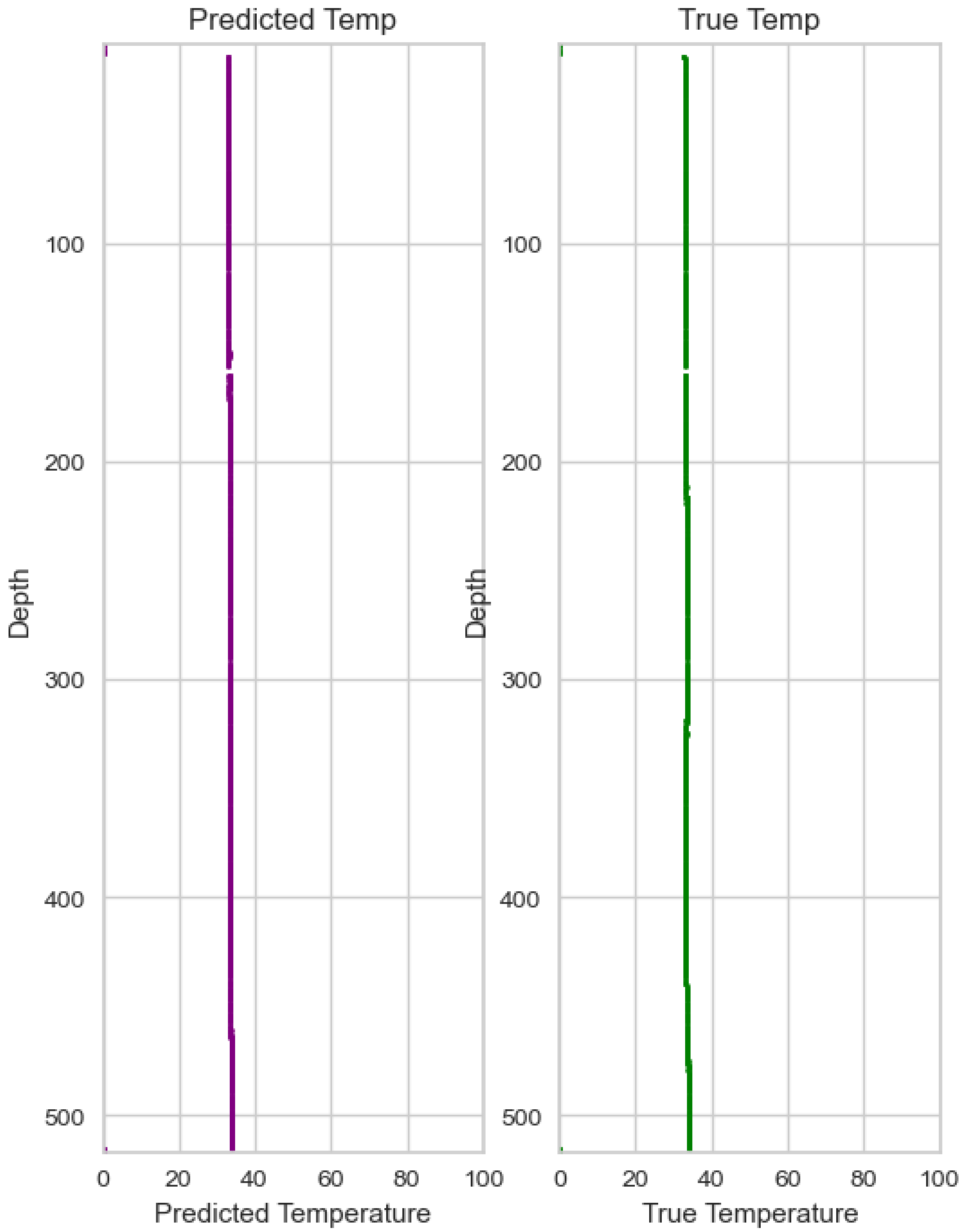

Figure 20. Predicted vs. actual temperature of RAH-17 well based on XG Boost algorithms.

4.2. Magnetic Data Interpretation

Figure 21 shows the TMI magnetic map over the HR volcanic field. It can be observed that some linear anomalies can be traced in the NW, trending on the west side of the HR volcanic field. It is well-known that a magnetic trend does not occur randomly; it is associated with a geologic structure. When analyzing the trends in the magnetic data, it can be recognized that minor trends can be seen on the eastern side of the HR volcanic field. In order to enhance the lineaments of the area of interest, an edge detection technique will be used, CET grid analysis.

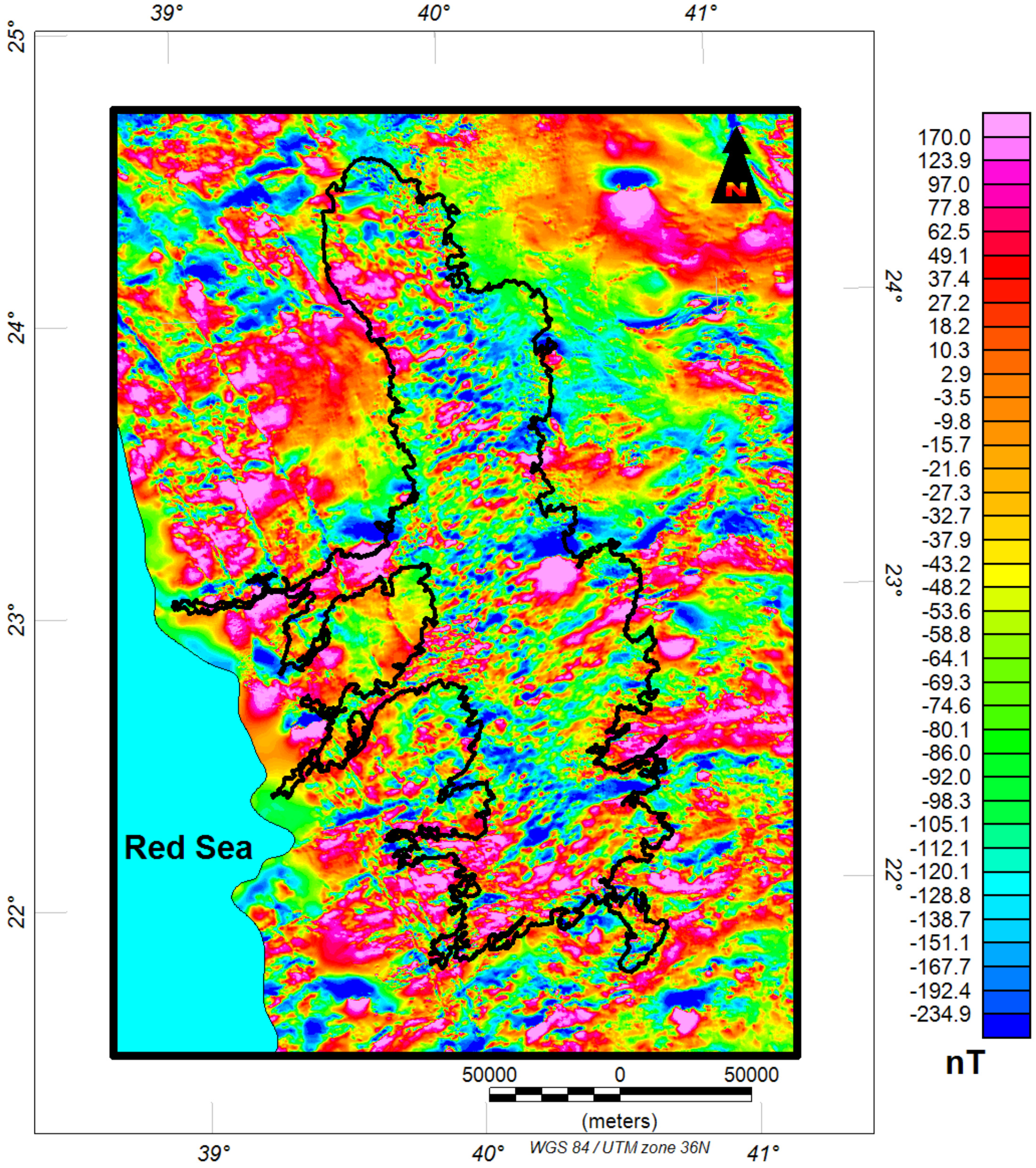

Figure 21. TMI of HR volcanic field and surrounding areas.

CET Grid Analysis

This tool is specifically designed for mineral exploration by geophysicists and geologists looking for discontinuities within magnetic and gravity data. The CET grid analysis provides a step-by-step trend detection menu which offers two different approaches to trend estimation. The first method, texture analysis-based image enhancement, is suitable for analyzing regions with subdued magnetic or gravity responses, where texture analysis can first enhance the local data contrast. The second method, discontinuity structure detection, is useful in identifying linear discontinuities and edge detection.

In the current study, we applied a CET filter to the TMI data in order to detect lineation/edges inside and outside of the HR volcanic field. Figures 22 and 23 show the results for where lineation (e.g., regional) inside and outside of the HR volcanic field was detected. It can be observed that the main trend for inside lineation is in the NE direction, while it is in the NW direction for the outside, as seen in the rose diagrams shown in Figures 24 and 25.

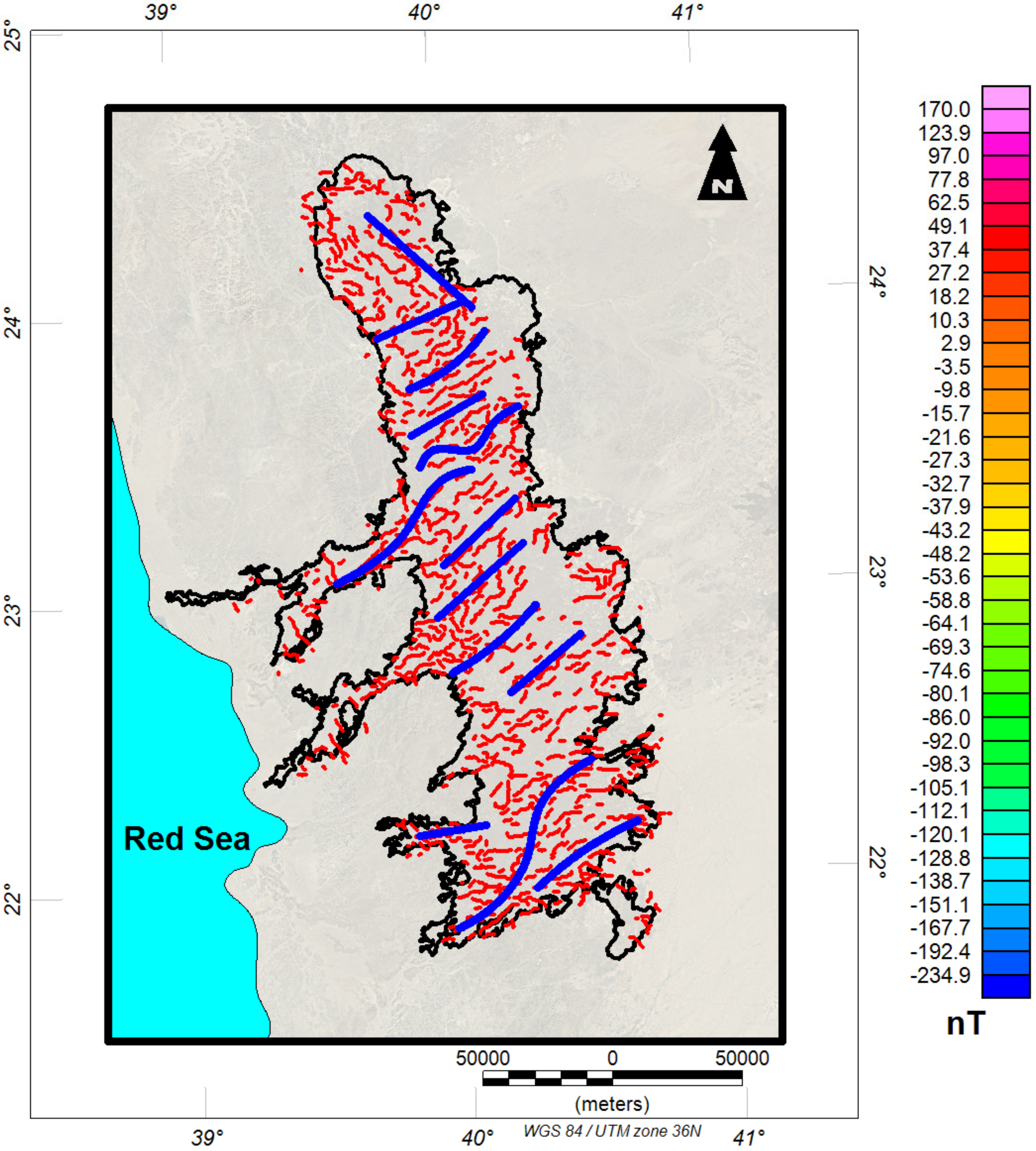

Figure 22. Major trends for inside the HR, from an analysis of magnetic data, are in blue color while the minor trends are in red color.

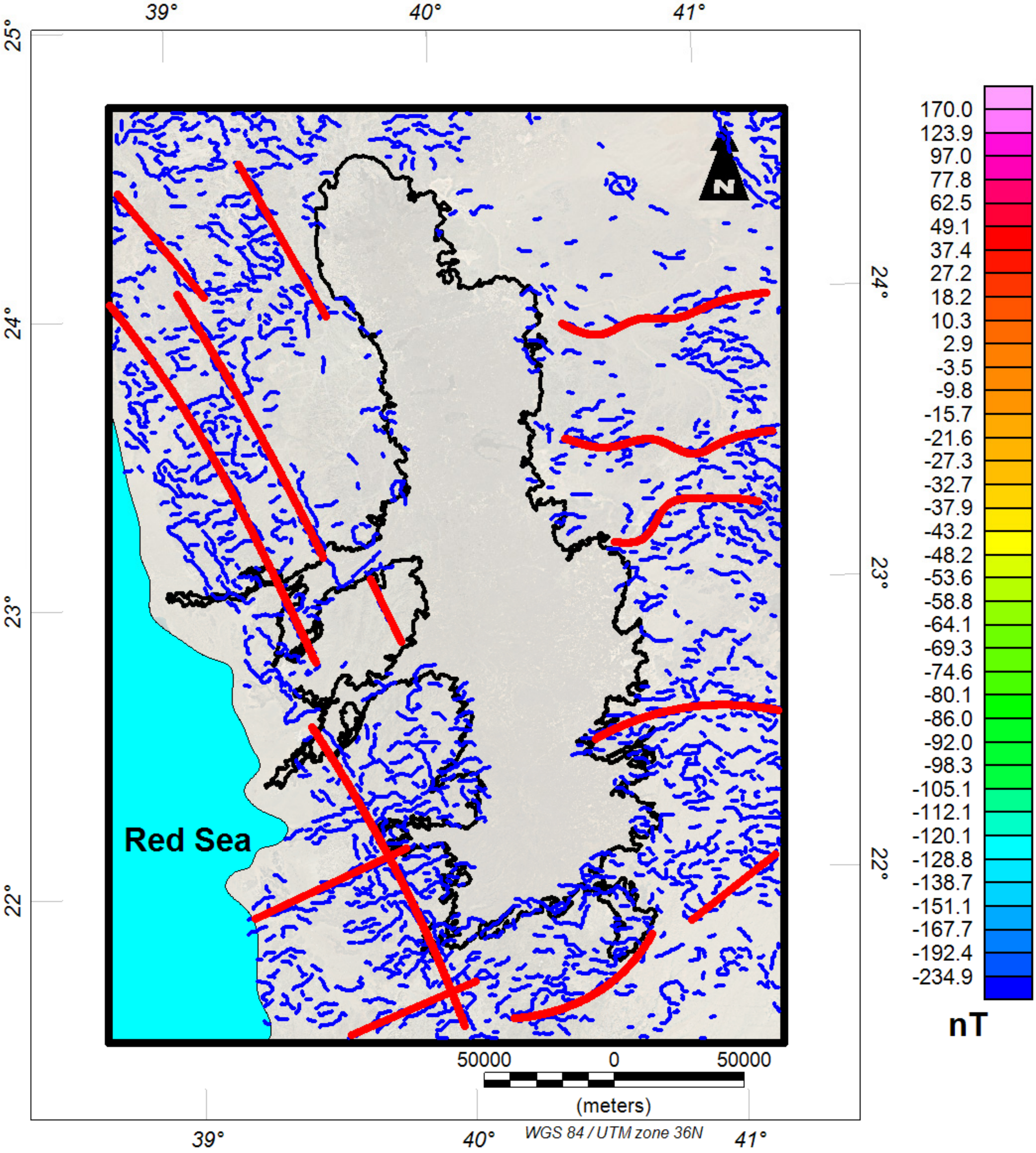

Figure 23. Major trends for the outside are in red color while the minor trends are in blue color.

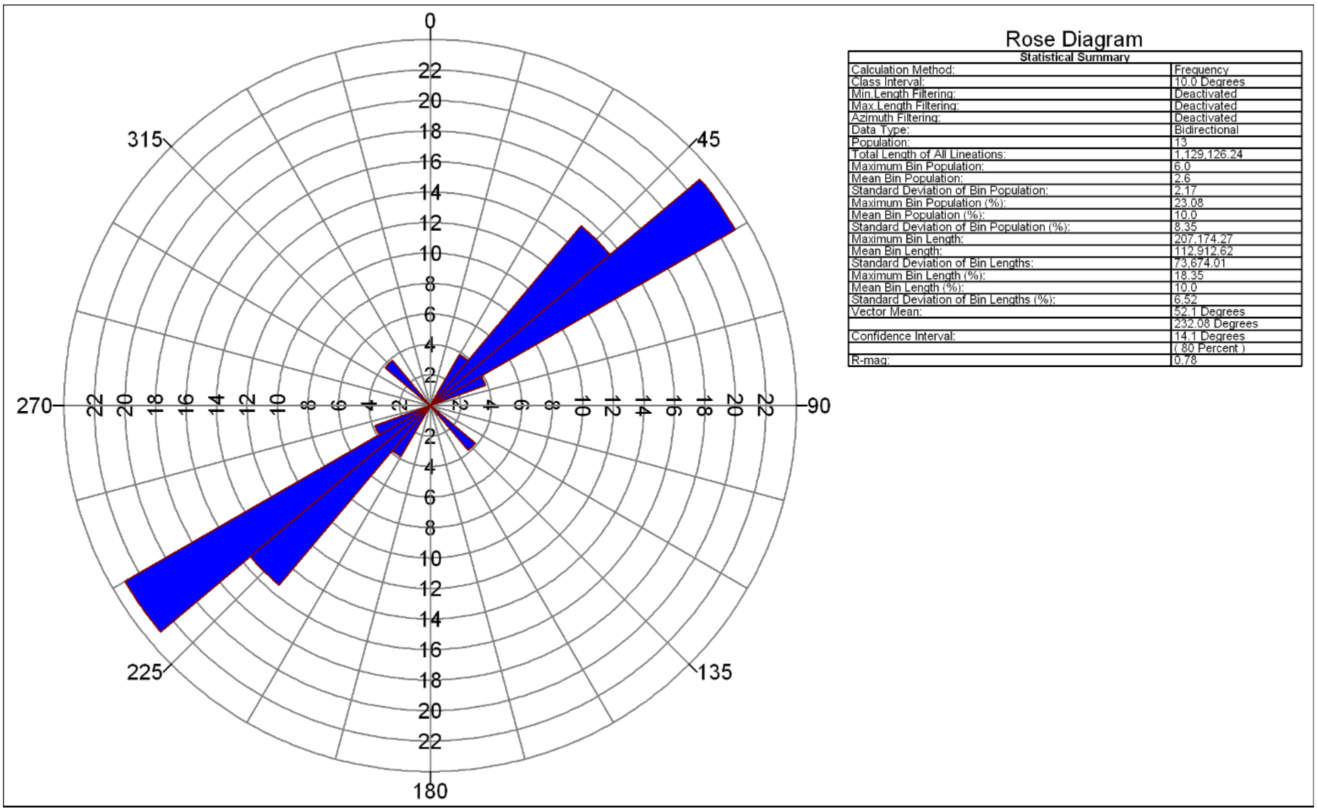

Statistical Summary	
Calculation Method:	Frequency
Class Interval:	10.0 Degrees
Min.Length Filtering:	Deactivated
Max.Length Filtering:	Deactivated
Azimuth Filtering:	Deactivated
Data Type:	Bidirectional
Population:	13
Total Length of All Lineations:	1,129,126.24
Maximum Bin Population:	6.0
Mean Bin Population:	2.6
Standard Deviation of Bin Population:	2.17
Maximum Bin Population (%):	23.08
Mean Bin Population (%):	10.0
Standard Deviation of Bin Population (%):	8.35
Maximum Bin Length:	207,174.27
Mean Bin Length:	112,912.62
Standard Deviation of Bin Lengths:	73,674.01
Maximum Bin Length (%):	18.35
Mean Bin Length (%):	10.0
Standard Deviation of Bin Lengths (%):	6.52
Vector Mean:	52.1 Degrees
	232.08 Degrees
Confidence Interval:	14.1 Degrees
	(80 Percent)
R-mag:	0.78

Figure 24. Rose diagram for major trends inside the HR volcanic field.

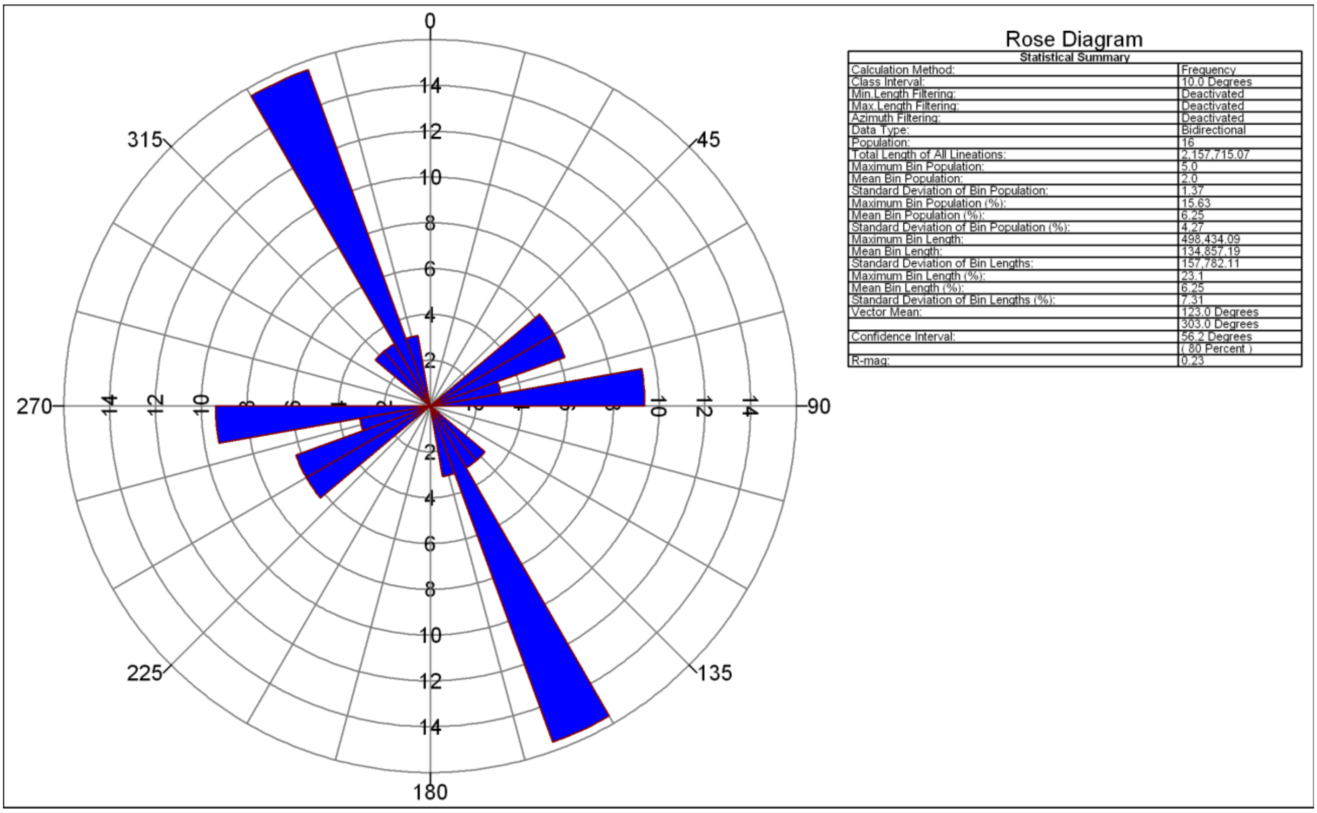

Statistical Summary	
Calculation Method:	Frequency
Class Interval:	10.0 Degrees
Min.Length Filtering:	Deactivated
Max.Length Filtering:	Deactivated
Azimuth Filtering:	Deactivated
Data Type:	Bidirectional
Population:	16
Total Length of All Lineations:	2,157,715.07
Maximum Bin Population:	5.0
Mean Bin Population:	2.0
Standard Deviation of Bin Population:	1.37
Maximum Bin Population (%):	15.63
Mean Bin Population (%):	6.25
Standard Deviation of Bin Population (%):	4.27
Maximum Bin Length:	498,434.09
Mean Bin Length:	134,857.19
Standard Deviation of Bin Lengths:	157,782.11
Maximum Bin Length (%):	23.1
Mean Bin Length (%):	6.25
Standard Deviation of Bin Lengths (%):	7.31
Vector Mean:	123.0 Degrees
	303.0 Degrees
Confidence Interval:	56.2 Degrees
	(80 Percent)
R-mag:	0.23

Figure 25. Rose diagram for major trends outside of the HR volcanic field.

It can be recognized that the main regional trend outside of the HR volcanic field is in the NW direction, parallel to the Red Sea, while inside the HR volcanic field it was in the NE direction. The two trends are perpendicular to each other, which means they have a direct relationship during the forming process.

The Red Sea is a tectonic rift zone which separates the Arabian Peninsula, on which the HR volcanic field is located, and the African Plate. This rift zone has resulted in the formation of several faults along the coastal sides. These faults are parallel and extend along the Red Sea. They can be easily recognized in Figure 23, which was obtained from the analysis of the magnetic data.

The majority of volcanic activity in the HR volcanic field is associated with the tectonic process occurring along the Red Sea rift, even the formation of the HR due to the Red Sea tectonic system.

These volcanic activities are represented by volcanic eruption and the flow of lava on the ground, and the formation of volcanic cones.

In addition, it can be recognized that the main faults inside the HR (Figure 24) are in the NE direction while the faults outside (Figure 25) are in the NW direction (parallel to the Red Sea), which implies that the formation of the HR was due to the Red Sea rift system, while the formation of faults inside the HR volcanic field were due to its local or small-scale tectonic activity.

4.3. LST and NDVI and CO_2 Emissions Interpretation

Integrating various datasets (such as geological, geophysical, field observation, geochemical, remote sensing, and drilling technologies) is necessary to effectively manage costs and reduce uncertainties in geothermal projects. RS offers a unique opportunity to streamline and reduce costs at each stage of geothermal project development, including the preliminary survey and potential site selection. RS data can be utilized to analyze surface manifestations of geothermal sites, including examining surface deformations related to geothermal activity, assessing gas emissions, and measuring surface temperature and heat flux. RS techniques are valuable for exploring and identifying fumaroles and hot springs through infrared analysis and surface topography. Although a wide range of exploration tools are available for geothermal prospecting, previous exploration strategies within the HR have been largely centered on geological and geophysical data interpretations. Generally, the identification of hydrothermal signatures related to geothermal prospects zones identification must be interpreted with care. However, for the effective and sustainable management of geothermal exploration programs, it is important to integrate spatial data as a means of identifying the most suitable location and its extent [8,72,73]. Satellite RS of thermal infrared radiation has proven effective in monitoring high-temperature volcanic features. Satellites were equipped with sensors operating in the visible, infrared, and thermal wavelength regions that could capture reflected and emitted radiation from the surface [74]. The LST has undergone a qualitative classification using the classification method described by [8,12] and presented in Table 3.

Table 3. LST indices were used to establish five qualitative classifications using satellite data [8,12].

Index	Temperature Range (°C)	Qualitative Classification
1	<39	Very Low
2	39–41	Low
3	41–43	Medium
4	43–50	High
5	>50	Very High

Geothermal exploration involves the identification of regions with high subsurface temperatures. One crucial parameter for such identification is the LST. In the current study, we examine the role of LST in exploring geothermal resources within HR. High LST values can indicate volcanic activity, such as the presence of lava flows or hot gases, which can cause an increase in LST. The HR volcanic field exhibited no active eruptions or significant volcanic activity between 2000 and 2021. A comprehensive geological investigation of mafic volcanism in the northernmost region of the HR volcanic field mapped 32 eruptive units, which erupted from around 1014 ± 14 ka to a single Holocene event in 1256 A.D. The lava flows in HR typically range from 10 to 15 km long, although some extend up to 23 km [24]. HR is a seismologically active area that experienced significant seismic activity and encountered a swarm of earthquake events in 1999 [7]. Therefore, any rise in LST recorded between 2000 and 2021 would likely be attributed to environmental factors rather than volcanic influences. LST data from 2021 would likely exhibit a noticeable increase in high LST as compared to 2000, as shown in Figure 26.

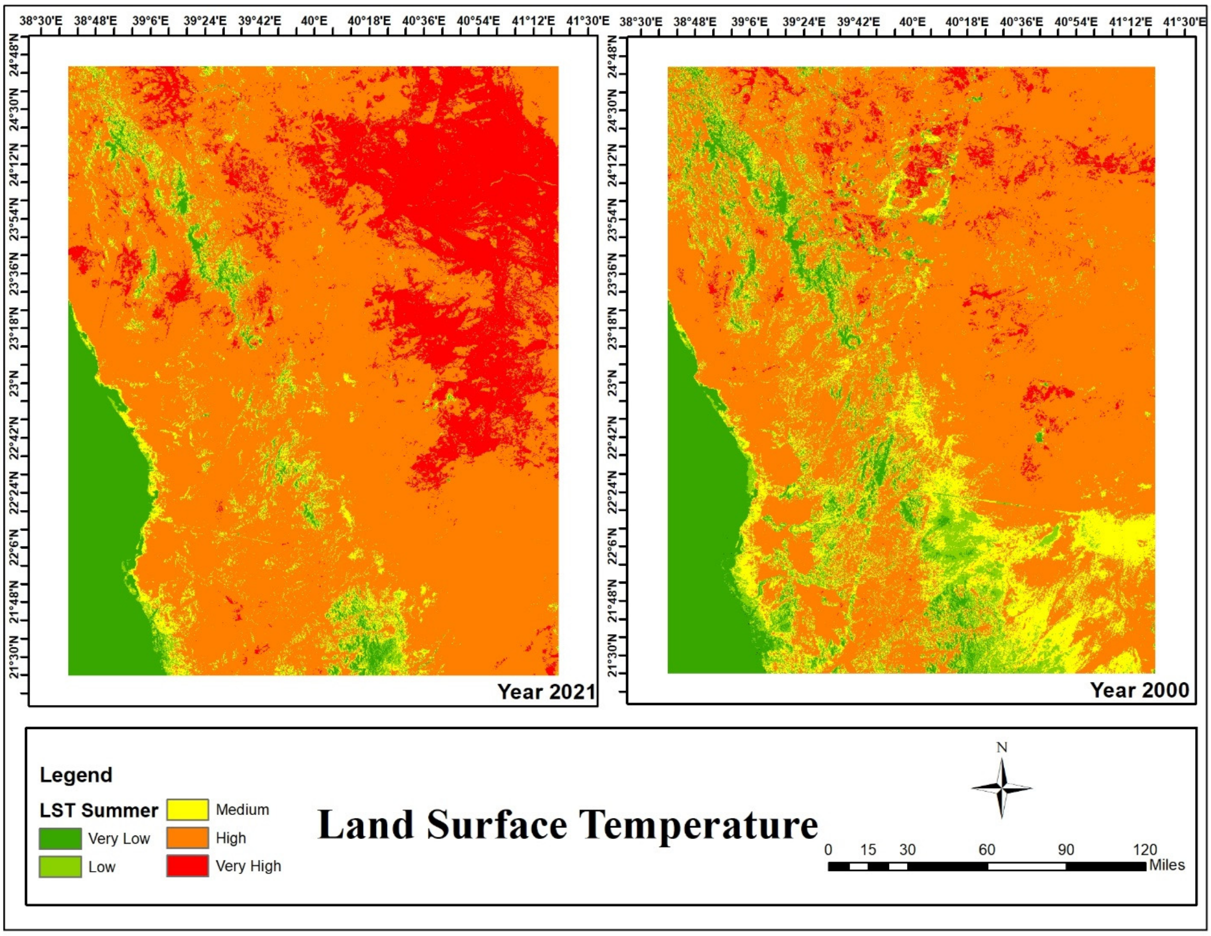

Figure 26. LST distribution map of the study area for 2000 and 2021.

The qualitative classifications of LST for the study area have determined that a maximum temperature-range data cluster lies within the high-to-very-high geothermal anomaly zones (Figure 26). The pie charts in Figure 27 present the qualitative classifications of LST for 2000 and 2021. In summary, it was concluded based on the qualitative classifications of LST that in 2021, 86% of the area falls within the high-to-very-high temperature zone, compared to 73% of the area in 2000, as shown in Table 4.

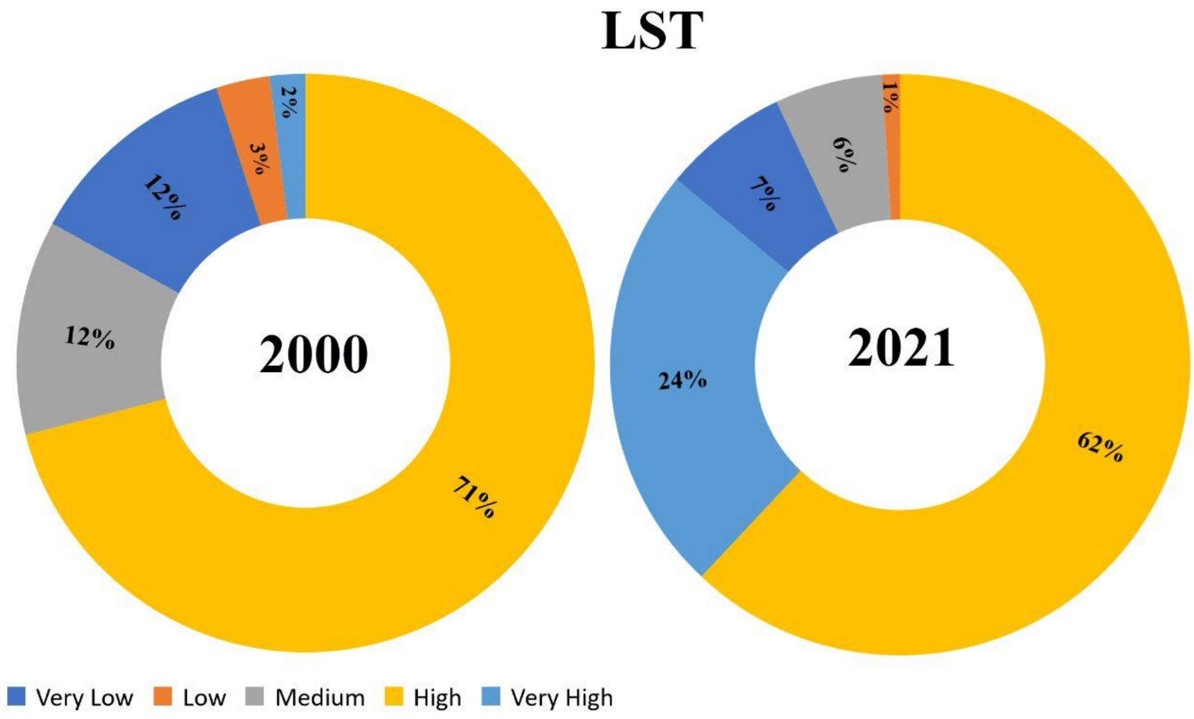

Figure 27. The comparative display of the qualitative classifications of LST for the years 2000 and 2021.

Table 4. A summary of statistical analysis of qualitative classifications of LST for the years 2000 and 2021.

Year	**Qualitative Classifications of LST**				
	Very High	**High**	**Medium**	**Low**	**Very Low**
2000	2%	71%	12%	3%	12%
2021	24%	62%	6%	1%	7%

The presence of very high LST values in the northeastern parts of the HR suggests the potential existence of geothermal resources in these areas. However, further geophysical exploration is highly recommended to assess this region's viability and development prospects. The presence of very high LST values in 2021 in a very small zone in the southwest parts of the HR suggests the potential existence of geothermal resources. Table 5 provides a comprehensive statistical analysis of LST and NDVI at various locations within HR for the years 2000 and 2021.

Table 5. Details of the statistical analysis of LST and NDVI of the HR volcanic field, considering a 100-sample point.

Year	**LST**				**NDVI**				**Correlation Coefficient for LST-NDVI**
	Min	**Max**	**Mean**	**Std**	**Min**	**Max**	**Mean**	**Std**	
2000	24.18	50.48	43.74	5.50	0.01	0.10	0.06	0.02	0.031
2021	28.42	53.81	46.36	5.24	0.01	0.13	0.07	0.02	0.095

RS was employed to gather data about an object and its surroundings from a considerable distance. RS techniques, such as LST and NDVI methods, are an alternative approach to detecting the presence of geothermal energy during geothermal exploration, addressing challenges related to time efficiency, economic feasibility, and accessibility to exploration sites. The high level of vegetation presents a challenge to accurately identifying geothermal conditions, due to its ability to absorb heat energy from geothermal surface features. This absorption results in lower LST recordings, impacting the geothermal identification process [58]. In this study, no vegetation is reported; almost 100% of the land is classified as bare soil based on the classification of NDVI, which categorizes three distinct types of surfaces based on their NDVI values: (a) bare soil (NDVI < 0.2), (b) mixed surface (0.2 > NDVI < 0.5), and (c) fully vegetation (NDVI > 0.5), as described in Figure 28 [8]. Figure 28 illustrates the variation in NDVI within HR for 2000 and 2021. It is worth noting that the entire area was classified as bare soil for the years 2000 and 2021, constituting almost 100% of the region, and a very limited area lies on the mixed surface on the northwest corner of the map.

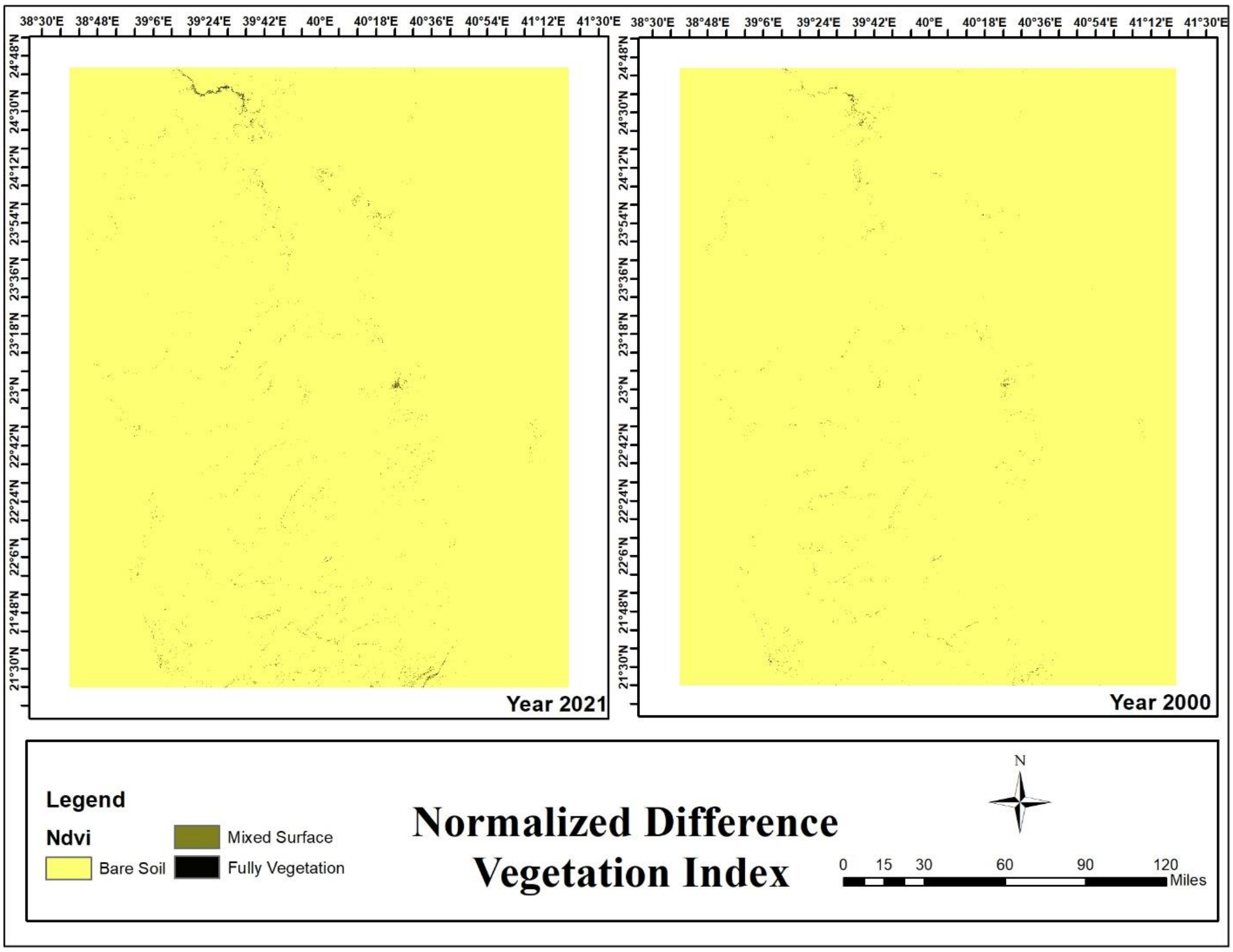

Figure 28. NDVI distribution map of the study area for 2000 and 2021.

The main primary sources of geogenic CO_2 emission are generally most elevated in thermal regions, which include the release of CO_2 from the magmatic mantle, degassing during metamorphic processes in active and dormant volcanoes and fault and fracture zones, geothermal systems, and CO_2-enriched groundwater [75,76]. In some cases, older volcanic regions may also experience the emission of CO_2 at low temperatures, but their contribution is very low. Indicators of CO_2 release include areas of disturbed or bare ground and the presence of a rotten egg-like odor, which is associated with the presence of H_2S. Globally, our understanding of the contribution of volcanic CO_2 is not as well-studied [75]. Volcanic and tectonic-related contributions account for less than 2% of anthropogenic emissions [77]. CO_2 is a prevalent gas emitted from volcanic areas. Changes in the release of CO_2 from the soil over time and space are valuable for identifying the locations of active faults and monitoring currently active volcanoes [78,79]. In addition to emissions from living organisms, geogenic CO_2 release typically originates from volcanic-magmatic, mantle-related, or metamorphic sources. The quantity of accessible CO_2 release data has grown, prompting a timely assessment of the existing findings concerning one another [80]. The distribution map in Figure 29 shows the CO_2 emission in the HR volcanic field, highlighting the hotspots (red color) associated with active volcanic activities and their connection to geothermal sources.

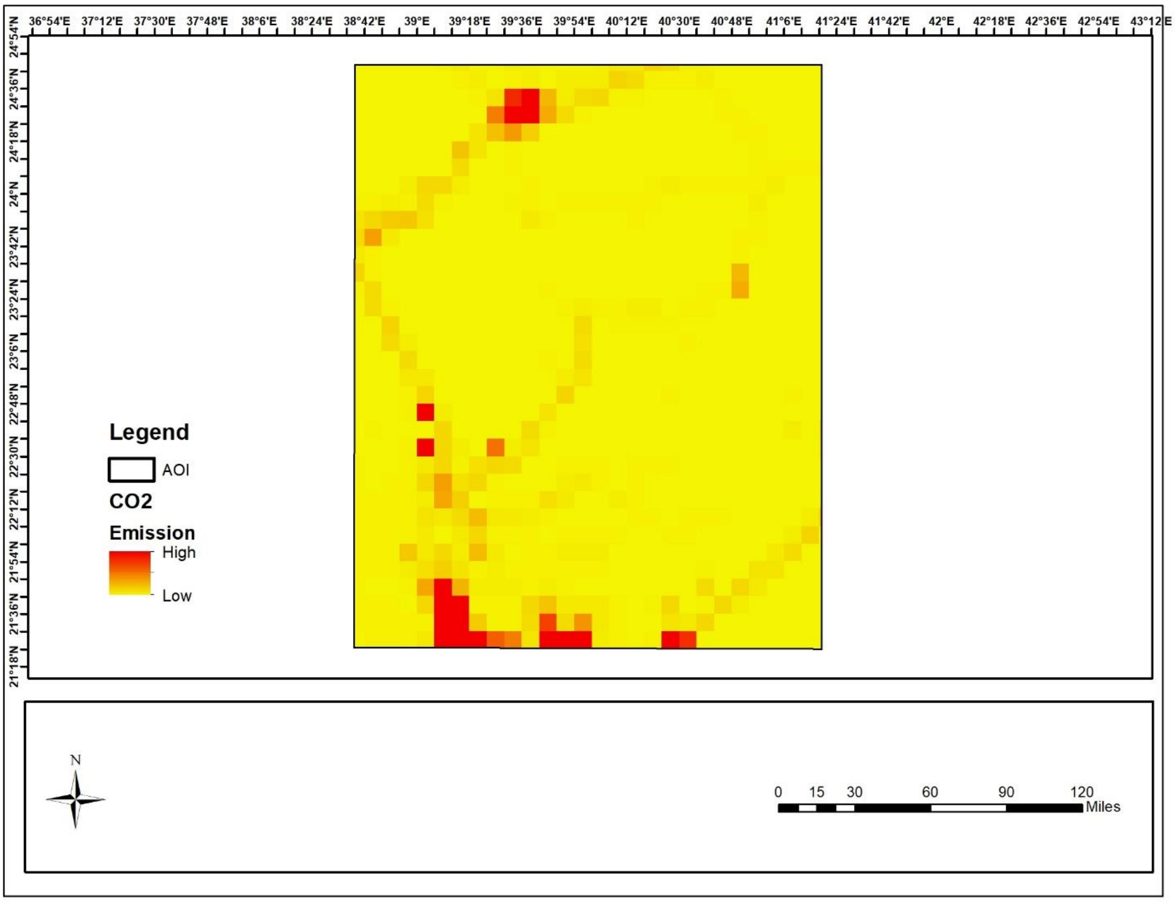

Figure 29. CO_2 emission distribution map of HR volcanic field.

5. Conclusions

This paper presents the land surface temperature and subsurface temperature distribution of the study area, revealing the existence of geothermal resources with different temperature ranges in the HR volcanic field. A crucial objective in advancing renewable energy resources is the spatial prediction of geothermal zones in HR. This region holds significant potential for geothermal energy production, particularly in the presence of deep faults. Cenozoic volcanoes contribute to the favorable conditions for geothermal energy exploitation in this area. The temperature logs confirm that the RAH-02, 07, 13, and 17 wells have geothermal potential, due to the maximum temperature range of around approximately 50 °C. It was concluded that the south portion of the study area shows the greatest geothermal potential because that zone had the highest temperature that was encountered. Geothermal resources are present in the subsurface, as verified by GG and HP results. We applied the CET filter to the TMI data in order to detect lineation/edges inside and outside the HR volcanic field; the results indicate that lineation (e.g., regional) inside and outside the HR volcanic field were detected. This study also examines thermal infrared imaging for geothermal prospecting and the monitoring of thermal activity in HR. LST and

NDVI analysis results indicate that the recorded temperatures range from 24.18 to 53.81 °C, while the area exhibits bare soil with NDVI values ranging from 0.01 to 0.13. Therefore, regions with temperatures greater than 43 °C are the best geothermal spots. The predicated data found the HR region to be the best candidate with its high volcanic activity. CO_2 emissions in the HR volcanic field highlight the hotspots associated with active volcanic activities and their connection to geothermal sources. In summary, it can be inferred that HR is abundant in geothermal resources, and the results presented in this paper provide crucial information for identifying and prioritizing areas with high geothermal potential for future exploration and development.

6. Future Research

Geothermal resources from volcanic fields like the Harrat volcanic field can provide a sustainable and renewable energy source in the KSA. It is recommended that advanced exploration techniques and acquisition methods are needed to further evaluate these resources' potential. Three-dimensional (3D) seismic data are required for a detailed knowledge of the subsurface geometry of the geothermal reservoirs. Drilling a test exploratory well to confirm the presence of high-temperature fluids and assess their flow rates could provide valuable data about the subsurface conditions and help estimate the potential energy output. It is suggested to perform a reservoir characterization study to analyze the properties of the geothermal reservoir, such as permeability and the porosity of rocks, to understand the fluids' behavior and optimize the geothermal system's design using 3D seismic data and advanced well logs data. Furthermore, the evaluation of core data is also essential for a better understanding of these reservoirs' potential.

Supplementary Materials: The following supporting information can be downloaded at: https://www.mdpi.com/article/10.3390/su151712718/s1, Figure S1: Pair plot without removal of the outlier of RAH-13 Well; Figure S2: Pair plot after removal of the outlier of RAH-13 Well.

Author Contributions: Conceptualization, N.N.E.-M.; methodology, M.E. and M.F.A.; software, Z.N.; formal analysis, M.A.; resources, F.A. and E.A.; data curation, N.N.E.-M.; writing—original draft, M.E. and Z.N.; writing—review and editing, M.E.; supervision, E.A.; project administration, M.A.; funding acquisition, F.A. All authors have read and agreed to the published version of the manuscript.

Funding: This research work was funded by the Institutional Fund Projects under grant no. IFPNC-001-145-2020.

Institutional Review Board Statement: Not applicable.

Informed Consent Statement: Not applicable.

Data Availability Statement: The data presented in this study are available upon request from the corresponding author.

Acknowledgments: This research work was funded by the Institutional Fund Projects under grant no. IFPNC-001-145-2020. Therefore, the authors gratefully acknowledge the technical and financial support from the Ministry of Education and King Abdulaziz University, Jeddah, Saudi Arabia.

Conflicts of Interest: The authors declare no conflict of interest.

References

1. Lund, J.W.; Toth, A.N. Direct utilization of geothermal energy 2020 worldwide review. *Geothermics* **2020**, *90*, 101915. [CrossRef]
2. Ng'Ethe, J.; Jalilinasrabady, S. GIS-based multi-criteria decision making under Silica Saturation Index (SSI) for selecting the best direct use scenarios for geothermal resources in Central and Southern Rift Valley, Kenya. *Geothermics* **2023**, *109*, 102656. [CrossRef]
3. Murdock, H.E.; Gibb, D.; Andre, T.; Sawin, J.L.; Brown, A.; Ranalder, L.; Andre, T.; Brown, A.; Collier, U.; Dent, C.; et al. *Renewables 2021—Global Status Report*; REN21 Secretariat: Paris, France, 2021; 603p, ISBN 978-3-948393-03-8.
4. Ren, P.R.S. *Renewables 2022 Global Status Report*; REN21 Secretariat: Paris, France, 2022. Available online: https://www.ren21.net/gsr-2022/ (accessed on 3 March 2023).
5. Putriyana, L.; Daud, Y.; Saha, B.B.; Nasruddin, N. A comprehensive data and information on low to medium temperature geothermal resources in Indonesia: A review. *Geéomeéch. Geophys. Geo-Energy Geo-Resour.* **2022**, *8*, 58. [CrossRef]

6. Aboud, E.; Alqahtani, F.; Elmasry, N.; Abdulfarraj, M.; Osman, H. Geothermal anomaly detection using potential field geophysical data in Raahat volcanic field, Madinah, Saudi Arabia. *J. Geol. Geophys.* **2022**, *11*, 1026.
7. Aboud, E.; Arafa-Hamed, T.; Alqahtani, F.; Marzouk, H.; Elbarbary, S.; Abdulfaraj, M.; Elmasry, N. The geothermal magmatic system at the northern Rahat volcanic field, Saudi Arabia, revealed from 3D magnetotelluric inversion. *J. Volcanol. Geotherm. Res.* **2023**, *437*, 107794. [CrossRef]
8. Alqahtani, F.; Aboud, E.; Ehsan, M.; Naseer, Z.; Abdulfarraj, M.; Abdelwahed, M.F.; El-Masry, N. Geothermal Exploration Using Remote Sensing, Surface Temperature, and Geophysical Data in Lunayyir Volcanic Field, Saudi Arabia. *Sustainability* **2023**, *15*, 7645. [CrossRef]
9. Lashin, A.; Bassam, A.; Arifi, A.; Rehman, N.; Faifi, A. In A Review of the Geothermal Resources of Saudi Arabia: 2015–2020. In Proceedings of the World Geothermal Congress 2020, Reykjavik, Iceland, 24–27 October 2020; pp. 1–12.
10. Al-Amri, A.M.; Abdelrahman, K.; Mellors, R.; Harris, D. Geothermal potential of Harrat Rahat, Northern Arabian Shield: Geological constraints. *Arab. J. Geosci.* **2020**, *13*, 268. [CrossRef]
11. Abdel-Fattah, M.I.; Shendi, E.H.; Kaiser, M.F.; Abuzied, S.M. Unveiling geothermal potential sites along Gulf of Suez (Egypt) using an integrated geoscience approach. *Terra Nova* **2020**, *33*, 306–319. [CrossRef]
12. Calderón-Chaparro, R.A.; Vargas-Cuervo, G. Determination of Hydrothermal Prospects in the Geothermal Region of Paipa (Boyacá, Colombia), Using Remote Sensing and Field Data. *Earth Sci. Res. J.* **2019**, *23*, 265–282. [CrossRef]
13. Abuzied, S.M.; Kaiser, M.F.; Shendi, E.-A.H.; Abdel-Fattah, M.I. Multi-criteria decision support for geothermal resources exploration based on remote sensing, GIS and geophysical techniques along the Gulf of Suez coastal area, Egypt. *Geothermics* **2020**, *88*, 101893. [CrossRef]
14. Mahwa, J.; Li, D.-J.; Ping, J.-H.; Leng, W.; Tang, J.-B.; Shao, D.-Y. Mapping the spatial distribution of fossil geothermal manifestations and assessment of geothermal potential of the Tangyin rift, Southeast of Taihang Mountain in China. *J. Mt. Sci.* **2022**, *19*, 2241–2259. [CrossRef]
15. Zaini, N.; Yanis, M.; Abdullah, F.; Van Der Meer, F.; Aufaristama, M. Exploring the geothermal potential of Peut Sagoe volcano using Landsat 8 OLI/TIRS images. *Geothermics* **2022**, *105*, 102499. [CrossRef]
16. Marwan; Yanis, M.; Muzakir; Nugraha, G.S. Application of QR codes as a new communication technology and interactive tourist guide in Jaboi, Sabang. *IOP Conf. Ser. Mater. Sci. Eng.* **2020**, *796*, 012025. [CrossRef]
17. Liu, S.; Ye, C.; Sun, Q.; Xu, M.; Duan, Z.; Sheng, H.; Wan, J. Detection of Geothermal Anomaly Areas with Spatio-Temporal Analysis Using Multitemporal Remote Sensing Data. *IEEE J. Sel. Top. Appl. Earth Obs. Remote Sens.* **2021**, *14*, 4866–4878. [CrossRef]
18. Chao, J.; Zhao, Z.; Lai, Z.; Xu, S.; Liu, J.; Li, Z.; Zhang, X.; Chen, Q.; Yang, H.; Zhao, X. Detecting geothermal anomalies using Landsat 8 thermal infrared remote sensing data in the Ruili Basin, Southwest China. *Environ. Sci. Pollut. Res.* **2022**, *30*, 32065–32082. [CrossRef]
19. Perozzi, L.; Guglielmetti, L.; Moscariello, A. Minimizing geothermal exploration costs using machine learning as a tool to drive deep geothermal exploration. In Proceedings of the 3rd Hydrocarbon Geothermal Cross Over Technology Workshop, Geneva, Switzerland, 9–10 April 2019.
20. Shahdi, A.; Lee, S.; Karpatne, A.; Nojabaei, B. Exploratory analysis of machine learning methods in predicting subsurface temperature and geothermal gradient of Northeastern United States. *Geotherm. Energy* **2021**, *9*, 18. [CrossRef]
21. Stelten, M.E.; Downs, D.T.; Champion, D.E.; Dietterich, H.R.; Calvert, A.T.; Sisson, T.W.; Mahood, G.A.; Zahran, H. The timing and compositional evolution of volcanism within northern Harrat Rahat, Kingdom of Saudi Arabia. *GSA Bull.* **2019**, *132*, 1381–1403. [CrossRef]
22. Camp, V.E.; Roobol, M.J. The Arabian continental alkali basalt province: Part I. evolution of Harrat Rahat, Kingdom of Saudi Arabia. *Geol. Soc. Am. Bull.* **1989**, *101*, 71–95. [CrossRef]
23. Moufti, M.R.; Németh, K. The Intra-Continental Al Madinah Volcanic Field, Western Saudi Arabia: A Proposal to Establish Harrat Al Madinah as the First Volcanic Geopark in the Kingdom of Saudi Arabia. *Geoheritage* **2013**, *5*, 185–206. [CrossRef]
24. Downs, D.T.; Robinson, J.E.; Stelten, M.E.; Champion, D.E.; Dietterich, H.R.; Sisson, T.W.; Zahran, H.; Hassan, K.; Shawali, J. *Geologic Map of the Northern Harrat Rahat Volcanic Field, Kingdom of Saudi Arabia*; US Geological Survey: Reston, VA, USA, 2019. [CrossRef]
25. Runge, M.G.; Bebbington, M.S.; Cronin, S.J.; Lindsay, J.M.; Kenedi, C.L.; Moufti, M.R.H. Vents to events: Determining an eruption event record from volcanic vent structures for the Harrat Rahat, Saudi Arabia. *Bull. Volcanol.* **2014**, *76*, 804. [CrossRef]
26. Abdelwahed, M.F.; El-Masry, N.; Moufti, M.R.; Kenedi, C.L.; Zhao, D.; Zahran, H.; Shawali, J. Imaging of magma intrusions beneath Harrat Al-Madinah in Saudi Arabia. *J. Asian Earth Sci.* **2016**, *120*, 17–28. [CrossRef]
27. Saibi, H.; Mogren, S.; Mukhopadhyay, M.; Ibrahim, E. Subsurface imaging of the Harrat Lunayyir 2007–2009 earthquake swarm zone, western Saudi Arabia, using potential field methods. *J. Asian Earth Sci.* **2019**, *169*, 79–92. [CrossRef]
28. Yao, Z.; Mooney, W.D.; Zahran, H.M.; Youssef, S.E.-H. Upper mantle velocity structure beneath the Arabian shield from Rayleigh surface wave tomography and its implications. *J. Geophys. Res. Solid Earth* **2017**, *122*, 6552–6568. [CrossRef]
29. Mellors, R.J.; Camp, V.E.; Vernon, F.L.; Al-Amri, A.M.S.; Ghalib, A. Regional waveform propagation in the Arabian Peninsula. *J. Geophys. Res. Solid Earth* **1999**, *104*, 20221–20235. [CrossRef]
30. Chang, S.-J.; Merino, M.; Van der Lee, S.; Stein, S.; Stein, C.A. Mantle flow beneath Arabia offset from the opening Red Sea. *Geophys. Res. Lett.* **2011**, *38*. [CrossRef]

31. Park, Y.; Nyblade, A.A.; Rodgers, A.J.; Al-Amri, A. Upper mantle structure beneath the Arabian Peninsula and northern Red Sea from teleseismic body wave tomography: Implications for the origin of Cenozoic uplift and volcanism in the Arabian Shield. *Geochem. Geophys. Geosyst.* **2007**, *8*. [CrossRef]
32. Siler, D.L.; Faulds, J.E.; Hinz, N.H.; Dering, G.M.; Edwards, J.H.; Mayhew, B. Three-dimensional geologic mapping to assess geothermal potential: Examples from Nevada and Oregon. *Geotherm. Energy* **2019**, *7*, 2. [CrossRef]
33. Fernàndez, M.; Berástegui, X.; Puig, C.; García-Castellanos, D.; Jurado, M.J.; Torné, M.; Banks, C. Geophysical and geological constraints on the evolution of the Guadalquivir foreland basin, Spain. *Geol. Soc. Lond. Speéc. Publ.* **1998**, *134*, 29–48. [CrossRef]
34. Salem, A.; Ravat, D.; Smith, R.; Ushijima, K. Interpretation of magnetic data using an enhanced local wavenumber (ELW) method. *Geophysics* **2005**, *70*, L7–L12. [CrossRef]
35. Youssef, M.A. Estimating and interpretation of radioactive heat production using airborne gamma-ray survey data of Gabal Arrubushi area, Central Eastern Desert, Egypt. *J. Afr. Earth Sci.* **2016**, *114*, 67–73. [CrossRef]
36. Bücker, C.; Rybach, L. A simple method to determine heat production from gamma-ray logs. *Mar. Pet. Geol.* **1996**, *13*, 373–375. [CrossRef]
37. Asfahani, J. Phosphate Prospecting Using Natural Gamma Ray Well Logging in the Khneifiss Mine, Syria. *Explor. Min. Geol.* **2002**, *11*, 61–68. [CrossRef]
38. Liu, Q.; Zhang, L.; Zhang, C.; He, L. Lithospheric thermal structure of the North China Craton and its geodynamic implications. *J. Geodyn.* **2016**, *102*, 139–150. [CrossRef]
39. Cooper, G.; Cowan, D. Enhancing potential field data using filters based on the local phase. *Comput. Geosci.* **2006**, *32*, 1585–1591. [CrossRef]
40. Litjens, G.; Kooi, T.; Bejnordi, B.E.; Setio, A.A.A.; Ciompi, F.; Ghafoorian, M.; van Der Laak, J.A.; Van Ginneken, B.; Sánchez, C.I. A survey on deep learning in medical image analysis. *Med. Image Anal.* **2017**, *42*, 60–88. [CrossRef]
41. Cox, V. *Translating Statistics to Make Decisions*; Apress: New York, NY, USA, 2017. [CrossRef]
42. Williamson, D.F.; Parker, R.A.; Kendrick, J.S. The Box Plot: A Simple Visual Method to Interpret Data. *Ann. Intern. Med.* **1989**, *110*, 916–921. [CrossRef]
43. Choubey, S.; Karmakar, G.P. Artificial intelligence techniques and their application in oil and gas industry. *Artif. Intell. Rev.* **2020**, *54*, 3665–3683. [CrossRef]
44. Ullah, J.; Li, H.; Ashraf, U.; Heping, P.; Ali, M.; Ehsan, M.; Asad, M.; Anees, A.; Ren, T. Knowledge-based machine learning for mineral classification in a complex tectonic regime of Yingxiu-Beichuan fault zone, Sichuan basin. *Geoenergy Sci. Eng.* **2023**, *229*, 212077. [CrossRef]
45. Bukar, I.; Adamu, M.B.; Hassan, U. A Machine Learning Approach to Shear Sonic Log Prediction. In Proceedings of the SPE Nigeria Annual International Conference and Exhibition, Lagos, Nigeria, 5–7 August 2019. [CrossRef]
46. Zahran, H.M.; Stewart, I.C.F.; Johnson, P.R.; Basahel, M.H. *Aeromagnetic-Anomaly Maps of Central and Western Saudi Arabia*; Saudi Geological Survey Open-File Report SGS-OF-2002-8; Saudi Geological Survey: Riyadh, Saudi Arabia, 2003; p. 6.
47. Hase, D.H. *Qualitative Analysis of Airborne Magnetometer Data: The Arabian Shield, Kingdom of Saudi Arabia*; US Geological Survey: Reston, VA, USA, 1970. [CrossRef]
48. Johnson, P.R.; Vranas, G.J. *Qualitative Interpretation of Aeromagnetic Data for the Arabian Shield*; Ministry of Petroleum and Mineral Resources, Directorate General of Mineral: Riyadh, Saudi Arabia, 1992.
49. Corporation, P. *The Interpretation of an Aeromagnetic Survey of the Cover Rocks Region, Kingdom of Saudi Arabia*; Saudi Arabian Deputy Ministry for Mineral Resources DMMR: Riyadh, Saudi Arabia, 1985.
50. Georgel, J.-M.; Bobillier, J.; Delom, J.; Bourlier, M.; Gelot, J.-L. *Total-Intensity Aeromagnetic Maps of the Precambrian Shield Reduced to the Pole and Upwards Continued to 800 m above Ground Level*; Saudi Arabian Directorate General of Mineral Resources DGMR Open-File Report BRGM-OF-09-15; Saudi Arabian Directorate General of Mineral Resources DGMR: Riyadh, Saudi Arabia, 1990.
51. Griscom, A. *An Aeromagnetic Interpretation of Eleven Map Sheets, Scale 1:250,000, in the Southern Tuwayq Quadrangles*; Saudi Arabian Deputy Ministry for Mineral Resources DMMR Open-File Report USGS-OF-02-70; Saudi Arabian Deputy Ministry for Mineral Resources DMMR: Riyadh, Saudi Arabia, 1982.
52. Hall, S.A. *A Total Intensity Magnetic Anomaly Map of the Red Sea and Its Interpretation*; US Geological Survey: Reston, VA, USA, 1979; pp. 1–260.
53. Kovesi, P. Symmetry and asymmetry from local phase. *Citeseer* **1997**, *190*, 2–4.
54. Kovesi, P. Image features from phase congruency. *Videre J. Comput. Vis. Res.* **1999**, *1*, 1–26.
55. Holden, E.-J.; Dentith, M.; Kovesi, P. Towards the automated analysis of regional aeromagnetic data to identify regions prospective for gold deposits. *Comput. Geosci.* **2008**, *34*, 1505–1513. [CrossRef]
56. Holden, E.-J.; Kovesi, P.; Dentith, M.C.; Wedge, D.; Wong, J.C.; Fu, S.C. Detection of Regions of Structural Complexity within Aeromagnetic Data Using Image Analysis. In Proceedings of the 25th International Conference of Image and Vision Computing New Zealand, Queenatown, New Zealand, 8–9 November 2010; pp. 1–8. [CrossRef]
57. Lam, L.; Lee, S.-W.; Suen, C.Y. Thinning methodologies-a comprehensive survey. *IEEE Trans. Pattern Anal. Mach. Intell.* **1992**, *14*, 869–885. [CrossRef]
58. Syawalina, R.K.; Ratihmanjari, F.; Saputra, R.A. *Identification of the Relationship between LST and NDVI on Geothermal Manifestations in a Preliminary Study of Geothermal Exploration Using Landsat 8 OLI/TIRS Imagery Data Capabilities: Case Study of Toro, Central Sulawesi*; Standford University: Stanford, CA, USA, 2022; pp. 1–8.

59. Eric, K.C. Using Landsat-8 Data in Preliminary Exploration for Geothermal Resources. *Int. J. Sci. Res. Sci. Eng. Technol.* **2019**, *6*, 223–240. [CrossRef]
60. Elbarbary, S.; Zaher, M.A.; Saibi, H.; Fowler, A.-R.; Saibi, K. Geothermal renewable energy prospects of the African continent using GIS. *Geotherm. Energy* **2022**, *10*, 8. [CrossRef]
61. Zhao, F.; Peng, Z.; Qian, J.; Chu, C.; Zhao, Z.; Chao, J.; Xu, S. Detection of geothermal potential based on land surface temperature derived from remotely sensed and in-situ data. *Geo-Spat. Inf. Sci.* **2023**, 2178335. [CrossRef]
62. Wang, K.; Jiang, Q.-G.; Yu, D.-H.; Yang, Q.-L.; Wang, L.; Han, T.-C.; Xu, X.-Y. Detecting daytime and nighttime land surface temperature anomalies using thermal infrared remote sensing in Dandong geothermal prospect. *Int. J. Appl. Earth Obs. Geoinformation* **2019**, *80*, 196–205. [CrossRef]
63. Crippa, M.; Guizzardi, D.; Banja, M.; Solazzo, E.; Muntean, M.; Schaaf, E.; Pagani, F.; Monforti-Ferrario, F.; Olivier, J.G.J.; Quadrelli, R. *CO_2 Emissions of All World Countries*; Publications Office of the European Union: Luxembourg, 2022.
64. Burton, M.R.; Sawyer, G.M.; Granieri, D. Deep carbon emissions from volcanoes. *Rev. Mineral. Geochem.* **2013**, *75*, 323–354. [CrossRef]
65. Gerlach, T. Volcanic versus anthropogenic carbon dioxide. *Eos* **2011**, *92*, 201–202. [CrossRef]
66. Rabuffi, F.; Silvestri, M.; Musacchio, M.; Romaniello, V.; Buongiorno, M.F. A Statistical Approach to Satellite Time Series Analysis to Detect Changes in Thermal Activities: The Vulcano Island 2021 Crisis. *Remote Sens.* **2022**, *14*, 3933. [CrossRef]
67. Rehman, S.; Shash, A. Geothermal Resources of Saudi Arabia–Country Update Report. In Proceedings of the World Geothermal Congress 2005, Antalya, Turkey, 24–29 April 2005; pp. 24–29.
68. Husain, T.; Khalil, A.A. Environment and Sustainable Development in the Kingdom of Saudi Arabia: Current Status and Future Strategy. *J. Sustain. Dev.* **2013**, *6*, p14. [CrossRef]
69. Asseng, S.; Ewert, F.; Martre, P.; Rotter, R.P.; Lobell, D.B.; Cammarano, D.; Kimball, B.A.; Ottman, M.J.; Wall, G.W.; White, J.W.; et al. Rising temperatures reduce global wheat production. *Nat. Clim. Chang.* **2015**, *5*, 143–147. [CrossRef]
70. Garcia-Gutierrez, A.; Espinosa-Paredes, G.; Hernandez-Ramirez, I. Study on the flow production characteristics of deep geothermal wells. *Geothermics* **2002**, *31*, 141–167. [CrossRef]
71. Jordan, T.E.; Richards, M.C.; Horowitz, F.G.; Camp, E.; Smith, J.D.; Whealton, C.A.; Stedinger, J.R.; Hornbach, M.J.; Frone, Z.S.; Tester, J.W.; et al. *Low Temperature Geothermal Play Fairway Analysis for the Appalachian Basin: Phase 1 Revised Report November 18, 2016*; Cornell University: Ithaca, NY, USA, 2016. [CrossRef]
72. Moraga, J.; Duzgun, H.; Cavur, M.; Soydan, H. The Geothermal Artificial Intelligence for geothermal exploration. *Renew. Energy* **2022**, *192*, 134–149. [CrossRef]
73. Witter, J.B.; Trainor-Guitton, W.J.; Siler, D.L. Uncertainty and risk evaluation during the exploration stage of geothermal development: A review. *Geothermics* **2018**, *78*, 233–242. [CrossRef]
74. Corradino, C.; Amato, E.; Torrisi, F.; Del Negro, C. Data-Driven Random Forest Models for Detecting Volcanic Hot Spots in Sentinel-2 MSI Images. *Remote Sens.* **2022**, *14*, 4370. [CrossRef]
75. Werner, C.; Fischer, T.P.; Aiuppa, A.; Edmonds, M.; Cardellini, C.; Carn, S.; Chiodini, G.; Cottrell, E.; Burton, M.; Shinohara, H.; et al. *Carbon Dioxide Emissions from Subaerial Volcanic Regions*; Cambridge University Press: Cambridge, UK, 2019; pp. 188–236. [CrossRef]
76. Tiwari, S.K.; Gupta, A.K.; Asthana, A.K.L. Evaluating CO2 flux and recharge source in geothermal springs, Garhwal Himalaya, India: Stable isotope systematics and geochemical proxies. *Environ. Sci. Pollut. Res.* **2020**, *27*, 14818–14835. [CrossRef] [PubMed]
77. Fischer, T.P.; Aiuppa, A. AGU Centennial Grand Challenge: Volcanoes and Deep Carbon Global CO_2 Emissions from Subaerial Volcanism—Recent Progress and Future Challenges. *Geochem. Geophys. Geosyst.* **2020**, *21*, e2019GC008690. [CrossRef]
78. Sun, Y.; Guo, Z.; Liu, J.; Du, J. CO2 diffuse emission from maar lake: An example in Changbai volcanic field, NE China. *J. Volcanol. Geotherm. Res.* **2018**, *349*, 146–162. [CrossRef]
79. Walia, V.; Lin, S.J.; Fu, C.C.; Yang, T.F.; Hong, W.-L.; Wen, K.-L.; Chen, C.-H. Soil–gas monitoring: A tool for fault delineation studies along Hsinhua Fault (Tainan), Southern Taiwan. *Appl. Geochem.* **2010**, *25*, 602–607. [CrossRef]
80. Girault, F.; Viveiros, F.; Silva, C.; Thapa, S.; Pacheco, J.E.; Adhikari, L.B.; Bhattarai, M.; Koirala, B.P.; Agrinier, P.; France-Lanord, C.; et al. Radon signature of CO2 flux constrains the depth of degassing: Furnas volcano (Azores, Portugal) versus Syabru-Bensi (Nepal Himalayas). *Sci. Rep.* **2022**, *12*, 10837. [CrossRef]